

The evolution of dust attenuation in $z \approx 2\text{--}12$ galaxies observed by JWST

Received: 23 March 2024

Accepted: 28 October 2024

Published online: 27 November 2024

 Check for updates

Vladan Markov^{1,2}✉, Simona Gallerani¹✉, Andrea Ferrara¹✉,
Andrea Pallottini¹, Eleonora Parlanti¹, Fabio Di Mascia¹,
Laura Sommovigo^{1,3} & Mahsa Kohandel¹

A sizable fraction of the heavy elements synthesized by stars in galaxies condenses into submicrometre-sized solid-state particles known as dust grains. Dust produces a wavelength-dependent attenuation, A_λ , of the galaxy emission, thereby substantially altering its observed properties. Locally, A_λ is in general the sum of a power law and a ultraviolet feature ('bump') produced by small, carbon-based grains. However, scant information exists regarding its evolution across cosmic time. Here, leveraging data from 173 galaxies observed by the James Webb Space Telescope in the redshift range $z = 2\text{--}12$, we report the detection of the ultraviolet bump in a $z \approx 7.55$ galaxy (when the Universe was only ~700 Myr old) and show that the power-law slope and the bump strength decrease towards high redshifts. We propose that the flat A_λ shape at early epochs is produced by large grains newly formed in supernova ejecta, which act as the main dust factories at such early epochs. Importantly, these grains have undergone minimal reprocessing in the interstellar medium due to the limited available cosmic time. This discovery offers crucial insights into the redshift-dependent evolution of dust attenuation properties, shedding light on the role of supernovae-driven dust production, grain size distribution at early cosmic times and the processes driving dust evolution at later epochs.

Dust attenuation refers to the absorption and scattering of photons along the line of sight (LOS) due to the intervening interstellar medium (ISM) dust. The shape of the dust attenuation curve, A_λ , in galaxies (that is, the slope of the curve and the strength of the characteristic ultraviolet (UV) bump at ~2,175 Å) is determined by both the intrinsic dust properties (mass, grain size distribution, chemical composition) and the spatial distribution of dust with respect to stars. In the case of simple dust-to-star geometry, for example, a point-like background source with a uniform dust screen, the loss of light along the LOS is instead referred to as 'dust extinction', which is governed solely by the intrinsic dust properties^{1,2}.

The slope of the attenuation curve is determined by the grain size distribution and chemical composition^{3–5}. In particular, a shift towards smaller (larger) grains results in steeper (shallow) shapes⁵.

Likewise, the rise of the characteristic UV bump feature at 2,175 Å is typically associated with the existence of small carbonaceous dust grains^{4,6}, including polycyclic aromatic hydrocarbons^{7,8}. The V-band attenuation, A_V , which serves as a proxy of the galaxy dust content along the LOS, has been identified as one of the primary drivers of the shape of the dust attenuation law^{9,10}. Theoretical studies suggest that this correlation may arise from radiative transfer (RT) effects dependent on the amount and spatial distribution of dust relative to different stellar populations^{11,12}. For instance, the increasing complexity of the dust-to-star geometry flattens the slope of the dust attenuation curve and reduces the prominence of the UV bump, regardless of the initial dust extinction curve^{11,13}.

The dust attenuation/extinction laws of high- z sources remain largely unknown. Only a handful of early star-forming galaxies^{14–16},

¹Scuola Normale Superiore, Pisa, Italy. ²Faculty of Mathematics and Physics, University of Ljubljana, Ljubljana, Slovenia. ³Center for Computational Astrophysics, Flatiron Institute, New York, NY, USA. ✉e-mail: vladan.markov@fmf.uni-lj.si; simona.gallerani@sns.it; andrea.ferrara@sns.it

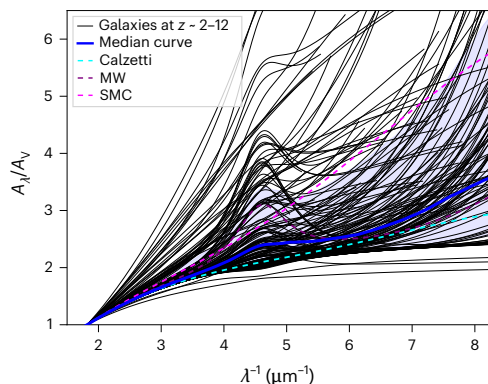


Fig. 1 | Dust attenuation curves for our full sample of galaxies at $z \approx 2$ –12, derived using our SED fitting method. Individual source curves are presented as black solid lines. The median curve and its 1σ dispersion (corresponding to 68% confidence interval (CI)) of the full sample are depicted as a blue solid line and the corresponding shaded region. The median attenuation curve and its 68% CI are derived from the 16th, 50th and 84th percentiles of a set of 5,000 attenuation curves that are generated using a bootstrapping approach (see ‘Attenuation curve parameterization’ section for details). For comparison, the empirical attenuation curves for Calzetti, the MW and the SMC are depicted as dashed lines in cyan, purple and magenta, respectively.

quasars^{17,18} and gamma-ray burst afterglows^{19,20} have constrained dust curves. Dust laws at high- z are expected to deviate from the well-established empirical dust curves of the local galaxies, such as the ‘Calzetti’²¹ attenuation curve for local starbursts and the Small Magellanic Cloud (SMC)²² and the Milky Way (MW) extinction curves²³. This redshift (z) evolution may arise from several factors such as distinct dust formation processes^{24,25} and dust reprocessing mechanisms^{26,27} occurring in the more extreme ISM conditions^{28–32} of early galaxies. Additionally, galaxies at intermediate^{33,34} and high- z (refs. 35,36) tend to be less dusty and show a clumpier structure and irregular distribution of dust and gas with respect to stars, compared to nearby sources^{37–40}.

In this Article, we apply our customized version of the Bayesian Analysis of Galaxies for Physical Inference and Parameter ESTimation (BAGPIPES) code^{15,41} to a large sample of star-forming galaxies at $z \approx 2$ –12, from the publicly available James Webb Space Telescope (JWST) spectroscopic observations, to investigate evolutionary trends of dust attenuation laws and their implications on the intrinsic dust properties and dust-to-star geometry.

Redshift evolution of dust attenuation law

We employ our customized version of BAGPIPES code^{15,41} to fit the individual spectra of a sample of 173 galaxies at $z \approx 2$ –12 observed by JWST. The code generates the best-fit model to the Near Infrared Spectrograph (NIRSpec) spectra and provides the best-fit parameters of the spectral energy distribution (SED) model from the medians of the posterior distribution. Outputs of the SED fitting process include fundamental physical characteristics of galaxies (stellar mass (M^*), star formation rate (SFR), metallicity (Z), mass-weighted stellar age ($\langle a \rangle_*^m$), ionization parameter (U) and V-band dust attenuation (A_V)) along with the properties of the dust attenuation model (c_1 – c_4 ; see the ‘SED fitting’ section for details). We utilize the c_1 – c_4 parameters to construct the dust attenuation curve for each galaxy. The inferred attenuation curves of our sample exhibit a wide diversity of slopes and UV bump strengths (Fig. 1 and the ‘Galaxy sample’ section). To explore potential trends in dust attenuation evolution, we split our sample in redshift bins by adopting equidistant cosmic time in each bin ($\Delta t \approx 0.5$ Gyr). The number of sources per bin varies in the 13–66 range.

Figure 2 depicts the median dust curves with the corresponding 1σ dispersion for each subsample. Although the associated uncertainties are relatively large, a noticeable trend emerges in the evolution of the

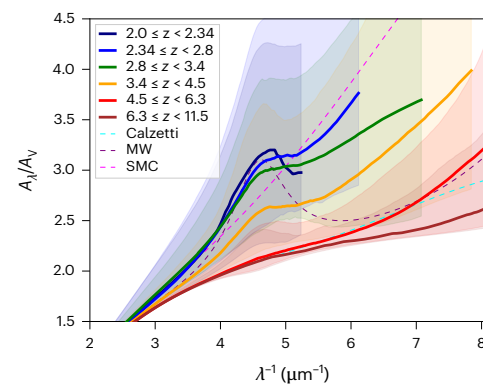


Fig. 2 | Dust attenuation curves for our full sample of galaxies at $z \approx 2$ –12 grouped by redshift. The median attenuation curves and their 1σ dispersion (68% CI) are shown as solid lines with corresponding shaded regions. The median curves and corresponding 68% CI are calculated using the 16th, 50th and 84th percentiles from a set of 5,000 attenuation curves generated through a bootstrapping approach (see ‘Attenuation curve parameterization’ section for details). The empirical curves of Calzetti, the MW and the SMC are represented by cyan, purple and magenta dashed lines, respectively.

dust attenuation curves with redshift. Specifically, with increasing redshift, the median slope flattens and the strength of the UV bump decreases.

To provide a more quantitative analysis of these results, we characterize the shape of the dust attenuation curve with the S and B parameters, which represent proxies for the UV-optical slope and the 2,175 Å bump strength, respectively². The slope is defined by the ratio of attenuation at 1,500 Å and the one in the V-band, $S = A_{1500}/A_V$. The UV bump strength is defined as $B = A_{\text{bump}}/A_{2,175}$, where A_{bump} is the additional attenuation above the baseline at 2,175 Å and $A_{2,175}$ is the total attenuation at 2,175 Å (see the ‘Attenuation curve parametrization’ section). The trends that we see in Fig. 2 remain apparent when we plot the UV-optical dust curve slope (S) and UV bump strength (B) separately, as functions of redshift (Fig. 3a,b, respectively).

Redshift evolution of the slope

Figure 3a illustrates the redshift evolution of the UV-optical slope (S) for each source of our full JWST sample and median values for subsamples grouped by redshift (as in Fig. 2). The median slope of $z \approx 2$ –3.5 galaxies approaches the SMC slope²². However, it gradually flattens with increasing redshift ($z \approx 3.5$ –5.5) and at $z > 5.5$ for galaxies is flatter than the MW slope²³. The median slopes of galaxies at intermediate- z are slightly steeper (although they are consistent within the 1σ uncertainties) with respect to most of the inferred slopes of various samples of intermediate- z galaxies from the literature. The discrepancy can be attributed to the fact that our overall JWST sample has a median A_V of -0.38. Conversely, the values of A_V for most galaxy samples in the literature are somewhat higher, $A_V \approx 0.9$ (ref. 42), $A_V \gtrsim 0.5$ (refs. 43–46), $A_V \approx 0.2$ –1.1 (ref. 47) and $A_V \approx 0.3$ –0.9 (ref. 48). Therefore, this difference in slopes is a consequence of a well-known trend wherein galaxies with low A_V tend to have steeper UV-optical slopes^{9,11,14}. If we instead restrict our JWST sample to more attenuated galaxies (with $A_V > 0.38$, Fig. 4a), our results are more aligned with the slopes inferred for known samples of $z \approx 1$ –3 galaxies. Additional potential origin of this discrepancy is discussed in the ‘Observational and model uncertainties’ section.

Figure 3a also depicts the best fit on the entire sample, whereas Fig. 4a shows the best fit on subsets of sources with $A_V \approx 0.1$ –0.38 and $A_V \geq 0.38$. We see that the slope of the attenuation curve (at fixed redshift) flattens with increasing A_V (despite notable uncertainties), as expected. This effect is more evident at lower redshifts ($z \lesssim 4$), whereas at $z \gtrsim 6$, the dust attenuation curves remain shallow and are largely unaffected by variations in A_V . Furthermore, the analysis of $A_\lambda(z)$ in

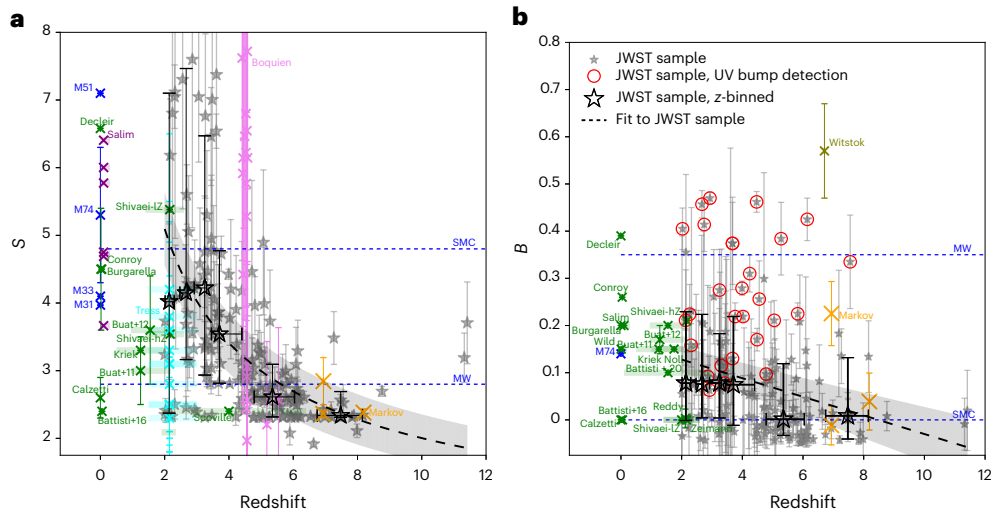


Fig. 3 | Dust attenuation parameters as a function of redshift. **a**, UV-optical slope (S) versus redshift. **b**, UV bump strength (B) versus redshift. The S and B medians and their 1σ dispersions for individual sources are shown as grey stars and error bars. These medians and 1σ dispersions are obtained using a bootstrapping approach that involves generating attenuation curves from a random sampling of c_1-c_4 from the posterior distribution ('Attenuation curve parametrization' section). Sources with a UV bump detection are highlighted by red circles. The median S and B values and their 1σ dispersions for galaxy subsets binned by redshift (corresponding to the redshift bins of Fig. 2) are indicated by

black stars and error bars. The median values and 1σ dispersions are estimated directly from the distribution of these parameters within each subset. The black dashed line and corresponding shaded region depict the best fit and 1σ s.e. for the entire sample, derived using the numpy polyfit function ('Attenuation curve parametrization' section). Literature results are depicted as coloured \times symbols with error bars representing their 1σ uncertainties ('Comparison with the literature' section). Corresponding horizontal stripes indicate the redshift range of galaxies for which the median/mean parameters have been estimated.

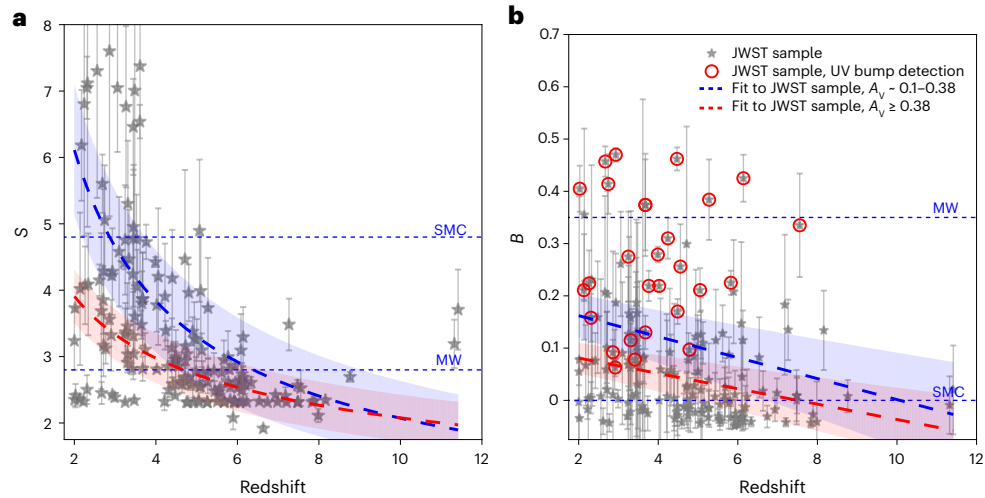


Fig. 4 | Dust attenuation parameters as a function of redshift, binned by their V-band attenuation A_v . **a**, UV-optical slope (S) versus redshift. **b**, UV bump strength (B) versus redshift. The S and B medians and their 1σ dispersions for individual sources are shown as grey stars and error bars. These medians and 1σ dispersions are obtained using a bootstrapping approach that involves generating attenuation curves from a random sampling of c_1-c_4 from the

posterior distribution ('Attenuation curve parametrization' section). The blue and red dashed lines and corresponding shaded regions depict the best fit and 1σ s.e. for subsets of sources with $A_v \approx 0.1-0.38$ (86 sources) and $A_v \geq 0.38$ (87 sources), respectively, derived using the numpy polyfit function ('Attenuation curve parametrization' section).

different A_v ranges shows that the flattening trend towards high- z persists irrespective of the A_v values considered. This implies that A_v is not the driver of the redshift evolution of the slope. Additionally, we examine if the flattening trend stems from an underlying dependence on other galaxy properties (for example, M^* , SFR, Z , $\langle a \rangle_*^m$ and U), but the overall trends remain regardless of the considered parameters (Extended Data Figs. 1–5).

Redshift evolution of the UV bump strength

Figure 3b depicts the redshift evolution of the UV bump strength (B). Similarly to the observed trends with the slope S , B also exhibits a general

decrease as redshift increases. The median B value reaches levels comparable to -20–25% of the MW bump strength in the $z \approx 2-4$ range. This is comparable with the inferred B values of the intermediate- z galaxies found in the literature^{42,44}, although the uncertainties remain relatively high. To further support this result, we emphasize that if we characterize the UV bump strength using the c_4 parameter (equation (1) (ref. 49)), we observe comparable trends in the redshift evolution of the UV bump strength (Extended Data Fig. 6).

The presence of the UV bump has been confirmed with a significance level of $>3\sigma$ ($B/B^{\text{err}} > 3$) for 28 sources within the $z \approx 2-8$ range (marked by red open circles in Fig. 3b). This accounts for -16% of the

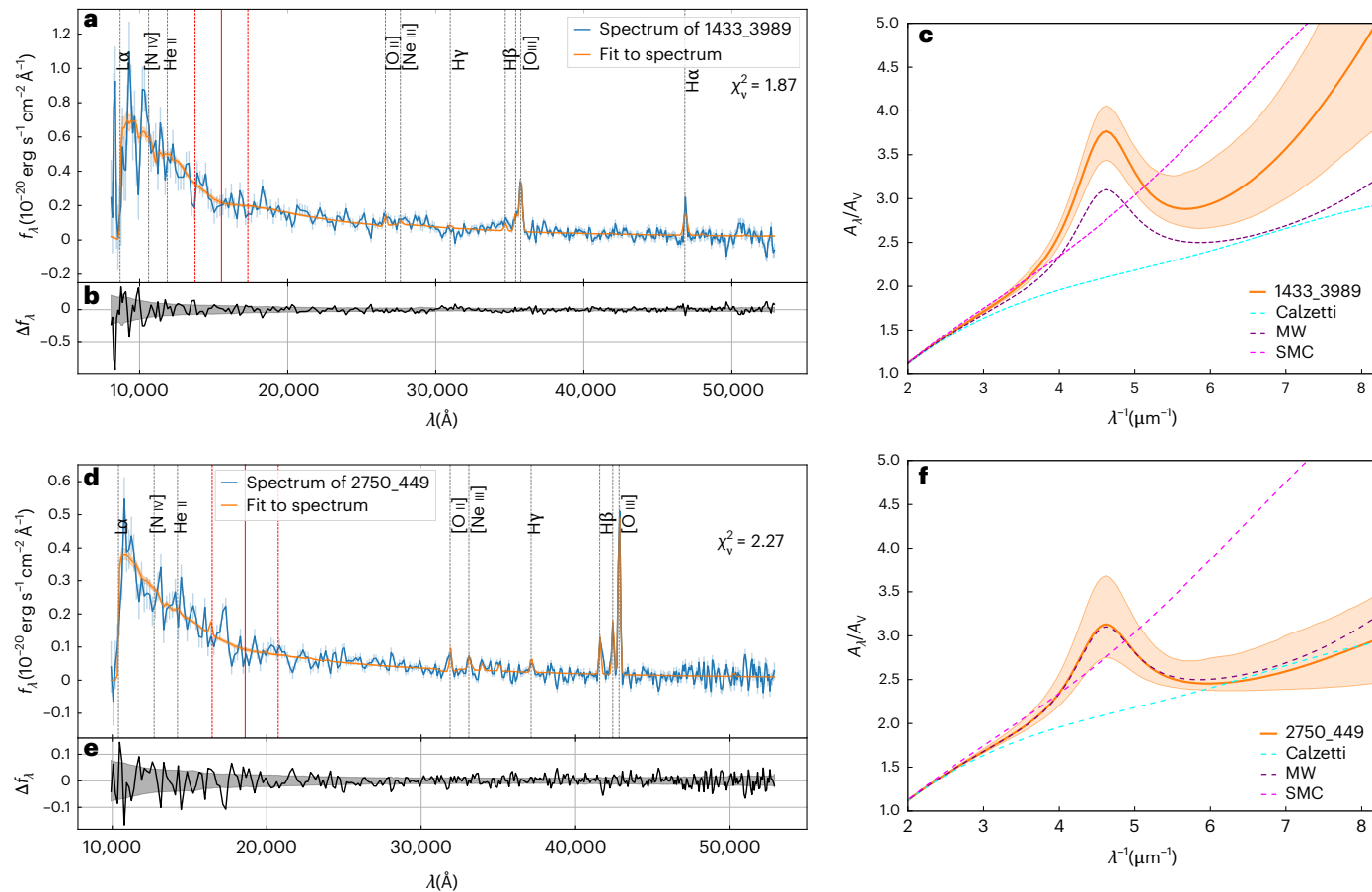


Fig. 5 | SED fitting results for two high-redshift sources exhibiting UV bump detection. **a,d**, SED fit for the 1433_3989 galaxy at $z \approx 6.14$ (**a**) and for 2750_449 at $z \approx 7.55$ (**d**). NIRSpec JWST spectra along with their corresponding 1σ s.e. are indicated in blue. The best-fit (median) posterior spectra along with their 1σ dispersions are indicated in orange. Vertical grey and red lines mark the positions of potential emission lines and the UV bump absorption feature of the spectrum. **b,e**, Residuals of the best fit on the observed spectrum, Δf_λ , with their 1σ s.e. for

1433_3989 (**b**) and for 2750_449 (**e**). **c,f**, The best-fit (median) dust attenuation curves with their 1σ dispersions for 1433_3989 (**c**) and for 2750_449 (**f**). The median and 1σ dispersion are estimated using a bootstrap method involving generating 5,000 attenuation curves from a random sampling of the c_1 – c_4 from the posterior. Dust model fits to the Calzetti, the MW and the SMC empirical curves are depicted as cyan, purple and magenta dashed lines, respectively.

full JWST sample. However, B is not well constrained and exhibits high uncertainties due to error propagation. If instead we use the c_4 parameter, which is better constrained as an output of the SED fitting procedure, we obtain a securely detected UV bump in ~21% of the sources (red open circles in Extended Data Fig. 6). This percentage (~21%) is consistent with previous results^{43,50} found in samples of $z \approx 1.0$ –2.5 galaxies. The median bump strength of sources with UV bump detection is $B \approx 0.7 \times B^{\text{MW}}$: that is, $c_4 \approx 0.75 \times c_4^{\text{MW}}$.

Applying both B and c_4 parameterizations, we confirm that the highest redshift galaxy of our JWST sample with a reliable UV bump detection is the 1433_3989 source at $z \approx 6.14$ (Fig. 5a–c). The UV bump strength for 1433_3989 is measured as $B = 0.43 \pm 0.05$ ($> 9\sigma$) or $c_4 = 0.083 \pm 0.014$ ($> 6\sigma$), which corresponds to a factor of -1.2 or -1.6 higher than the MW bump, depending on the considered parametrization. Moreover, the highest redshift source with a confirmed UV bump detection using only the B parameter is the 2750_449 source at $z \approx 7.55$ (Fig. 5d–f). The UV bump strength for 2750_449 is quantified as $B = 0.34 \pm 0.10$ ($> 3\sigma$) or $c_4 = 0.054 \pm 0.025$ ($> 2\sigma$) (that is, -0.95 or -1.05 of the MW bump).

Discussion

Our results show that the attenuation law evolves with redshift. Specifically, the attenuation slope flattens from $S > 4$ at $z \approx 2$ to $S \approx 2$ at $z > 8$. This trend is found independently of the value of A_v . Furthermore, the

strength of the UV bump decreases and eventually disappears at early epochs (from $B \approx 0.1$ at $z \approx 2$ –4 to $B \approx 0$ at $z > 5.5$).

We now turn to the interpretation of these findings. In principle, the observed evolutionary trends can be explained by three scenarios: RT effects dependent on (1) the amount of attenuation—that is, A_v ; or (2) dust distribution relative to stars of various ages; or (3) changes in the intrinsic dust properties (primarily grain size distribution and chemical composition). Although in general identifying the dominant factor is challenging⁵¹, the quality of the present data allows us to draw solid conclusions.

It is well established that smaller (larger) A_v values produce steeper (flatter) attenuation curves. Such correlation has been both predicted^{9,11,12} and observed^{2,52}. The physical interpretation is that, in the low- A_v (optically thin) limit, UV photons have a higher probability of being scattered and eventually absorbed, leading to the steepening of the slope^{9,53}. In the high- A_v (optically thick) limit, the shape of the curve is flattened by both scattering into the LOS and radiation from unobscured OB stars¹¹. Indeed, we also find (Fig. 4) that at fixed redshift, S increases with decreasing A_v . However, we do see that the flattening trend towards high- z persists irrespective of A_v . We can then rule out the first scenario.

Scenario (2) is based on the evidence that complex dust-to-star geometries flatten the slopes and reduce the UV bump strengths of dust attenuation curves^{11–13,54} as in those conditions UV photons from

young stars escape more easily. Although the detailed distribution of dust and gas in galaxies is often not easy to measure, a clumpy ISM structure is commonly reported for galaxies across the entire redshift range $z \approx 2$ –11.5 considered here^{37,38,55–57}. This suggests that the overall complex dust-to-star geometry at $z \approx 2$ –11.5 alone may not be sufficient to explain the observed trends in attenuation curves across the considered redshift range. Thus, scenario (2) seems unlikely.

Scenario (3) invokes changes in the grain properties. First, we note that our results are consistent with predictions from theoretical studies^{58–60} that have investigated the cosmological evolution of interstellar dust. A recent study⁶⁰ finds that, at a fixed metallicity, extinction curves flatten and the UV bump becomes less prominent with redshift. The study concluded that such trends are driven by a shift in the grain size distribution, favouring larger grains at early epochs. What causes such a shift?

The early prevalence of large grains could be attributed to dust production mechanisms in the ejecta of core-collapse Type II supernovae (SN II) (refs. 61–63). These dust sources are predicted to predominantly form large ($\sim 0.1 \mu\text{m}$) grains^{58,62–64}. Grains are then released into the ISM where they undergo shattering processes^{58–60,65}, breaking them into smaller units. However, shattering is a rather slow process, with typical timescales of $\gtrsim 0.5$ –1 Gyr^{58,64}. Consequently, the transition from large to smaller grains is gradual and is completed only by $z \approx 6$. Alternatively, small grains might be preferentially destroyed by Coulomb explosions in the presence of strong radiation fields^{66,67} like the ones present in early, compact galaxies.

The redshift evolution of S and B (or c_4) we find supports the third scenario. Importantly, the slope remains consistently shallow with a small dispersion at $z \gtrsim 5.5$. This might be interpreted with the existence of a single dominant dust formation channel (that is, SN II) in which large grains are formed and only minimally reprocessed in the ISM in the limited cosmic time available^{63,68}. The decrease of the bump strength towards high- z also supports this interpretation, as carbonaceous grains are scarce in SN II yields (~90% silicate and ~10% carbon dust)⁵⁹.

At $z \lesssim 5$ –5.5, a larger variety of attenuation curves is observed. This is likely due to a combination of several effects, including the transition from SN II to asymptotic giant branch stars^{69,70} as the dominant dust sources, dust growth in the ISM^{64,71}, more efficient shattering and sputtering^{58–60,65}. Concurrently, the UV bump emerges at $z \lesssim 5$ (around ~1.2 Gyr), marking the epoch when dust formation in asymptotic giant branch stars becomes dominant, leading to enhanced production of carbonaceous grains. Finally, a marginal decrease in both S and B at $z \lesssim 3.4$ may be attributed to processes such as coagulation and accretion becoming more prominent at later epochs^{59,65}.

In summary, the flattening of dust attenuation curves at high- z suggests that we might be observing galaxies through a curtain of dust newly formed in SN II ejecta, although other less-likely explanations cannot be completely excluded. Progress might come from cosmological hydrodynamic simulations including dust and related RT effects^{18,37,72}. These will make it possible to accurately determine the dust-to-star geometry, incorporate and explore different intrinsic dust properties (grain size distribution and chemical composition) and take into account RT effects. In parallel, insights into the intrinsic dust properties of high- z sources can be gained via observations of point-like sources, such as quasars^{17,73} and gamma-ray burst afterglows^{19,20}.

Methods

Spectroscopic data

We use publicly available NIRSpec data retrieved from the DAWN JWST Archive (DJA)⁷⁴, an initiative of the Cosmic Dawn Center. DJA includes all publicly available Cycle 1 and 2 spectroscopic and photometric observations from various JWST surveys. The data reduction of the NIRSpec data was performed entirely and uniformly with MSAEXP (tool for extracting JWST NIRSpec micro-shutter assembly (MSA) spectra⁷⁵) Python script, by the Cosmic Dawn Center.

Here, we focus on the analysis of NIRSpec prism spectra. The output one-dimensional (1D) spectra achieve wavelength-dependent resolution of $R \approx 30$ –300, ranging from $\lambda \approx 0.6$ to $\lambda \approx 5.3 \mu\text{m}$. This allows us to probe the nebular lines and continuum emission from rest-frame UV to infrared. However, due to the limited velocity resolution of $\gtrsim 1,000 \text{ km s}^{-1}$, we are unable to resolve nebular emission lines. A fraction of the spectral region below the wavelength of the Ly α line is selectively masked due to the potential contamination by the intervening neutral intergalactic medium.

Sample selection

Our target selection process closely follows the one outlined in our recent work¹⁵. We conduct a visual inspection of all grade 3 NIRSpec prism spectra, opting for galaxies exhibiting a prominent continuum and nebular line emission while excluding sources with strong negative features.

We select sources at $z > 2$ to ensure that we can effectively probe the rest-frame UV-optical wavelength range, allowing us to accurately constrain the shape of the dust attenuation curve and the potential presence of the UV bump. We further clean our sample by selecting spectra with an average channel signal-to-noise ratio > 3 , in the rest-frame wavelength range of 1925–2425 Å, corresponding to the peak position of the UV bump (2,175 Å). Additionally, we conduct a visual examination of the SED fits for all sources observed with NIRSpec. Any objects for which the SED models cannot yield a reasonable fit within the associated uncertainties are excluded from further consideration.

Finally, we exclude galaxies that exhibit negligible dust attenuation (that is, with $A_V \approx 0$) from our initial sample. For a galaxy to be considered ‘dusty’, it must meet two criteria: (1) V-band dust attenuation of $A_V > 0.1$; (2) $A_V > 0$ with a significance of $> 3\sigma (A_V/A_V^{\text{err}} > 3)$.

Galaxy sample

We ended up with a final sample of 173 ‘dusty’ galaxies. These galaxies fall within a spectroscopic redshift range of $2.0 \lesssim z \lesssim 11.4$, with a median redshift of $z \approx 4.5$, with stellar masses of $6.9 \lesssim \log M_*/M_\odot \lesssim 10.9$, SFRs $0.1 \lesssim \text{SFR per } M_\odot \text{ yr}^{-1} \lesssim 240$ and V-band dust attenuation $0.1 \lesssim A_V \lesssim 2.3$ (Supplementary Fig. 1).

Figure 1 depicts a large diversity of attenuation curves of our full JWST sample. For instance, the slopes range from those shallower than the Calzetti curve to the ones considerably steeper than the SMC curve. The strength of the UV bump varies considerably from curves in which it is completely absent (as in the SMC case) to those surpassing the bump strength observed in the MW. In Fig. 1 we also plot the median attenuation curve along with its 1σ uncertainties, computed from the full JWST sample. The median curve and its dispersion are derived using a bootstrapping approach.

Slit-loss correction

The flux values at a given wavelength reported in JWST NIRSpec MSA-based data may not always coincide with the ones reported in photometric data. The discrepancy between the NIRSpec MSA spectra and the photometric data can arise from several factors such as slit losses, flux calibration of both spectra and photometry and spectroscopic and photometric aperture. Slit loss refers to the reduction in the observed flux in spectroscopic data due to extension and off-centred location of the science target in the NIRSpec spectrograph shutters of finite dimensions (0.20 arc seconds \times 0.46 arc seconds)^{76,77}. The impact of slit loss is wavelength-dependent because the full width at half maximum (FWHM) of the point spread function widens with increasing wavelength.

To address the impact of slit loss and correct for the discrepancy between the NIRSpec spectra and the photometric data, we employ the following approach. First, we utilize the Python tool by DJA⁷⁴ to extract photometry from Hubble Space Telescope, JWST Near-Infrared Camera and JWST Near-Infrared Imager and Slitless Spectrograph, using

the right ascension, declination and redshift for each target. Next, we overlay the photometric points onto the spectrum for comparison. The discrepancy between the spectroscopic and photometric data is observed in 94% of the sources from our sample. It can reach up to a factor of 6–9 in the most extreme cases of very extended and/or off-centred sources. In case of a discrepancy, we correct the spectrum by dividing it with one of the throughputs provided by the JWST user documentation⁷⁶ until achieving a satisfactory alignment between the spectra and photometry.

To assess potential systematic uncertainties arising from the above-mentioned slit-loss-correction method reliant on visual inspection, we adopt an alternative approach to take into account slit losses. This method involves quantifying the discrepancy between photometric and spectroscopic flux density measurements for each source ($f_{\lambda}^{\text{phot}}/f_{\lambda}^{\text{spec}}$) and performing an uncertainty-weighted linear fit on these quantities. Subsequently, we utilize this linear regression function to correct the spectra affected by slit losses. By applying this reproducible and consistent methodology across our entire galaxy sample, we minimize potential inconsistencies and systematic errors. We find that our results closely mirror the initially reported redshift trends of dust attenuation curves (Figs. 2 and 3), as demonstrated in Supplementary Fig. 2.

Moreover, in Supplementary Fig. 3, we present the redshift trends of the attenuation curve, as well as the *S* and *B* parameters derived from SED fitting on spectra without correction for slit losses. In summary, our primary findings regarding the overall redshift trends of the slope (*S*) and the bump (*B*) remain consistent regardless of the application of slit-loss correction or the method employed for it.

Far infrared observations

Although an important portion of our sample sources is expected to exhibit sufficient brightness in the continuum emission within the far infrared (FIR) spectrum to be detectable with submillimeter facilities, given their typical SFR around $\text{SFR} \approx 4 M_{\odot} \text{yr}^{-1}$, we delved into the available Atacama Large Millimeter/submillimeter Array (ALMA) data. A considerable fraction of our sources (>60%) remained beyond the observational reach of ALMA due to their positioning in the northern sky, with $\delta > 20^\circ$. The remaining 69 sources of our JWST sample are distributed across the Great Observatories Origins Deep Survey (GOODS)-South (50), Abell 2744 (17) and RXJ 2129 (2) fields. These sources include 13 (17) sources exhibiting UV bump detections, based on the *B* (c_4) parameter.

Out of these 69 galaxies, ALMA data are available for 62 of them. Specifically, 49 out of 50 sources from GOODS-South were part of the GOODS-ALMA (2015.1.00543.S; principal investigator (PI): D. Elbaz)⁷⁸, ALMA Hubble Ultra Deep Field (2012.1.00173.S; PI: J. Dunlop)⁷⁹, Hubble Ultra Deep Field–Jansky Very Large Array (JVLA)–ALMA (2015.1.00098.S; PI: K. Kohno)⁸⁰ and GOODS-South (2017.1.00755.S; PI: D. Elbaz)⁸¹ 1.1–1.3 mm surveys. Additionally, 13 out of 17 Abell 2744 sources were surveyed in MOSAIC-D (2022.1.00073.S; PI: S. Fujimoto)⁸² and Abell_2744 (2018.1.00035.L; PI: K. Kohno)⁸³ studies. Finally, ALMA did not observe the two sources within the RXJ 2129 field. Despite the accessibility of ALMA data for these 62 sources, none of them have produced statistically significant detections across the various surveyed datasets.

SED fitting

In our recent study¹⁵, we presented a customized version of the BAGPIPES SED fitting code⁴¹ that enables us to simultaneously constrain the fundamental physical properties of galaxies (for example SFR, M_{\star} , Z) and the shape of their dust attenuation law. Our tool has been thoroughly tested on synthetic spectra attenuated by empirical dust curves¹⁵. In this section, we give a summary of our method.

BAGPIPES is a Bayesian SED fitting code that generates realistic galaxy spectra using the Stellar Population Synthesis models⁸⁴, nebular emission models precomputed with CLOUDY photoionization code⁸⁵

and intergalactic medium models⁸⁶. The Star Formation History (SFH) can be parameterized with various parametric and flexible SFH models. We employ the non-parametric SFH model with a ‘continuity’ prior as our fiducial SFH model, because it allows greater flexibility in fitting the ‘true’ SFHs and constraining less biased physical properties of galaxies, compared to parametric models^{15,87,88}.

The warm dust emission component within H II regions is included in CLOUDY, whereas the cold dust emission component within the neutral ISM is modelled with the grey body emission. The dust attenuation recipe includes a two-component dust screen model⁵⁴ to account for extra attenuation toward the stellar birth clouds. Dust attenuation can be modelled using standard empirical templates: ‘Calzetti’²¹ attenuation curve, SMC²² and MW extinction curves²³ and flexible dust models^{54,89}. We implement the analytical dust attenuation law⁴⁹ into BAGPIPES, and we use it as our fiducial dust attenuation model. The analytical form of the dust attenuation law, normalized by A_V , is

$$A_{\lambda}/A_V = \frac{c_1}{(\lambda/0.08)^{c_2} + (0.08/\lambda)^{c_3} + c_3} + \frac{233[1 - c_1/(6.88^{c_2} + 0.145^{c_3} + c_3) - c_4/4.60]}{(\lambda/0.046)^2 + (0.046/\lambda)^2 + 90} + \frac{c_4}{(\lambda/0.2175)^2 + (0.2175/\lambda)^2 - 1.95}, \quad (1)$$

where c_1, \dots, c_4 are dimensionless parameters and λ is the wavelength in micrometres. The three components of the Drude model describe the rise in far-UV attenuation, attenuation within the near-UV and optical spectrum and the 2,175 Å bump, respectively. The main advantage of this flexible dust model is its capability to replicate local empirical dust curves (Calzetti, MW, SMC), along with all the fundamental properties of (synthetic) galaxies¹⁵. Additionally, we note that the dust attenuation model flexibility enables the recovery of any potential variations in the dust attenuation laws of early galaxies¹⁵. This aspect is important in the case of high-redshift galaxies because there are no physical reasons to support the notion that dust attenuation curves in early epochs resemble any of the dust laws observed in the local Universe. In this work, we apply our tool to a large sample of high-redshift galaxies, and we showcase the flexibility of the dust model to capture large variations in both the slope of the attenuation curve and the UV bump strength. Nevertheless, it is important to note that the dust attenuation model sets the central wavelength and FWHM of the UV bump at fixed values of $\lambda_0 = 2,175 \text{ \AA}$ and FWHM $\approx 475 \text{ \AA}$, respectively. The central wavelength of the UV bump feature exhibits minimal variation, at least locally⁹⁰. Hence, fixing the central wavelength at 2,175 Å is a reasonable assumption to make. Nonetheless, several studies of the FWHM of the UV bump at intermediate redshifts ($z \approx 2$) have reported smaller FWHM values, of a factor of >2. This restriction might limit the model’s ability to capture variations of these UV bump parameters, which may be observed at higher redshift^{16,91}.

BAGPIPES is based on a Bayesian approach and the MultiNest nested sampling algorithm⁹². BAGPIPES requires that the instructions on the SED model be provided: that is, the parameters of the model components (for example, SFH, nebular emission and dust attenuation) and their priors. The prior probability distributions for each of the parameters of the model are given in Supplementary Table 1. In this work, the selected prior probability densities for model parameters are nearly identical to those of our initial work¹⁵. The priors on the dust attenuation parameters are carefully selected to encompass the parameter range of the dust model fit to Calzetti, SMC, LMC and MW templates, as well as any potential unconventional attenuation curve variations. However, the allowed prior limits on all parameters have been expanded to encompass a potentially wider parameter space that could be relevant for a larger galaxy sample spanning a substantially broader redshift range of $z \approx 2$ –12. For instance, prior limits are set

to allow super-solar metallicities (up to $Z \approx 2.5 Z_{\odot}$), high dust content ($A_v \approx 8$) and prominent UV bump ($c_4 \approx 0.1$). The prior limits of the UV bump parameter c_4 (related to B) are set as $-0.005 < c_4 < 0.1$. These limits are designed to accommodate the potential convergence of c_4 towards zero, a trait observed in certain well-known attenuation/extinction curves lacking a distinct UV bump, such as the SMC and Calzetti curves. As a result, there is a possibility for c_4 to occasionally yield slightly negative values during SED fitting (as seen in Extended Data Fig. 6). However, it is important to note that such negative values are most probably not indicative of any physical phenomenon but rather a consequence of the constraints imposed by our prior limits.

Statistical tests

To evaluate the quality of the fit, we initially rely on visual inspection to assess how accurately the SED model captures the features and trends present in the observed spectra. Additionally, we compute the residuals between the observed and modelled spectra, as illustrated in Fig. 5b,e.

Next, we adopt a frequentist χ^2 test approach for assessing the goodness of fit and consistency for Bayesian models from the SED fitting procedure⁹³. Specifically, we utilize the chi-square (χ^2) statistics. Here, χ^2 is defined as the difference between the observed and the modelled flux densities normalized by the observed errors:

$$\chi^2 = \sum_{i=1}^n \frac{(f_{\lambda}^{\text{obs}} - f_{\lambda}^{\text{model}})^2}{\sigma_{\text{obs}}^2}. \quad (2)$$

The reduced chi-square statistic $\chi^2_v = \chi^2/v$ represents the total chi-square of each source χ^2 , normalized by the degrees of freedom, v . The degrees of freedom are calculated as $v = n - k$, where n denotes the number of data points and k signifies the number of model parameters¹⁵ ($k = 16$ for our fiducial model; Supplementary Table 1). Our analysis reveals that the distribution of χ^2_v is in the range of $\chi^2_v = 4.1^{+0.3}_{-1.5}$. Notably, three sources exhibit $\chi^2_v > 100$, primarily due to particularly noisy spectra at shorter wavelengths ($\lambda_{\text{rf}} < 2,000 \text{ \AA}$). However, removing the high- χ^2_v sources does not affect the identified trends. Additionally, we present the χ^2_v measurements for two high- z sources showing UV bump detections at the highest redshifts (Fig. 5a,d).

We compared the quality of fits between our fiducial model, featuring a flexible analytical dust attenuation model, and a SED fitting model using a Calzetti-like dust attenuation template for our galaxy sample¹⁵. Our analysis shows that the fiducial model performs significantly better for 148 out of 173 sources (~86%), with a P value < 0.05 . The P value distribution is heavily skewed towards lower values, emphasizing the fiducial model's superior performance. Twenty-two sources (~13%) have a P value of 0.05–1, indicating that the fiducial model provides a better fit, but the improvement is not statistically significant. The fiducial model does not significantly enhance the fit for the remaining three sources (~2%), with a P value = 1. However, many sources with high P values exhibit a flat Calzetti-like curve (constrained by the analytical attenuation model). Additionally, a few sources show poorer SED fits due to noisy spectra in the rest-frame UV. Excluding sources with high P values from our analysis does not alter the inferred redshift trends.

Furthermore, we compared the fit to the spectra using the fiducial dust attenuation model and a bump-free model (with $c_4 = 0$) (ref. 15) for a subsample of 28 galaxies with a UV bump detection (right panel of Fig. 3). Our analysis shows that our fiducial model provides a significantly better fit for 24 out of 28 sources (~86%), with a P value < 0.05 . This includes both high-redshift sources with UV bump detection (Fig. 5). The P value distribution is notably skewed towards 0, once again emphasizing the enhanced performance of our fiducial model. For one source, a P value ≈ 0.2 indicates a somewhat better fit with the fiducial model. In the remaining three sources, the UV bump does not enhance the fit significantly (P value ≈ 1), but both models show poorer SED fits due to noisy spectra in the rest-frame UV.

Attenuation curve parametrization

To compare our constrained dust attenuation curves with those documented in the literature, we employ the parameterization introduced by ref. 2. The primary parameters of their work that provide information about the wavelength-dependent attenuation characteristics are the UV-optical slope (S) and UV bump strength (B) (ref. 2). The slope, S , is defined as $S = A_{1500}/A_v$, where A_{1500} is the attenuation at $\lambda = 1,500 \text{ \AA}$ and A_v is the attenuation in the V-band (that is, at $\lambda = 5,500 \text{ \AA}$).

The UV bump strength, B , is defined as $B = A_{\text{bump}}/A_{2175}$, where A_{bump} refers to the extra attenuation attributed to the bump above the baseline at $\lambda = 2,175 \text{ \AA}$ and A_{2175} is the total attenuation at $\lambda = 2,175 \text{ \AA}$. We note that in the original parametrization of the UV bump with the B parameter², the baseline at $2,175 \text{ \AA}$ is calculated using a relation derived from simulated attenuation curves¹¹ $A_{2175,0} = 0.33A_{1500} + 0.67A_{3000}$. In this work, we derive the $2,175 \text{ \AA}$ baseline by fitting the dust curve with an analytical dust model⁴⁹ and setting the c_4 parameter (which serves as a proxy for the UV bump strength) as $c_4 = 0$. This approach allows us to constrain the UV bump parameter B more precisely, with slightly reduced uncertainties.

In Figs. 1 and 2, the median attenuation curves and their 1σ dispersion (corresponding to 68% CI), are derived from the 16th, 50th and 84th percentiles of a set of 5,000 attenuation curves that are generated using a bootstrapping approach, which involves 5,000 random samples of the c_1 – c_4 parameters constrained for the given galaxy (sub)sample.

In Figs. 3 and 4 and Extended Data Figs. 1–5, the values of S and B for each galaxy (grey stars) are determined through the application of the dust attenuation model, $A_v/A_v = f(\lambda, c_1, c_2, c_3, c_4)$ (equation (1)), where the c_1 – c_4 parameters are the outputs of the SED fitting procedure (the 50th percentile of the posterior) for each source. Next, the uncertainties on S and B represent 1σ dispersion from the median values, estimated by employing a bootstrapping approach, which involves generating 100 attenuation curves A_v/A_v from a random sampling of the c_1 – c_4 parameters from the posterior for each source. In Fig. 3, the median values and 1σ dispersion of S and B parameters of subsets of galaxies grouped by redshift (black stars) are estimated directly from the distribution of these parameters within each subset.

In Figs. 3 and 4 and Extended Data Figs. 1–5, the slope–redshift and UV bump–redshift relations have the form $\log S = k_1 \log z + n_1$ and $B = k_2 z + n_2$. The best-fit values for the model parameters k_i and n_i , along with their 1σ uncertainties, are obtained using a numpy polyfit function, as

$$\log S = (-0.580 \pm 0.064) \log z + (0.882 \pm 0.042), \quad (3)$$

$$B = (-0.020 \pm 0.05)z + (0.167 \pm 0.025). \quad (4)$$

The uncertainties on the best-fit values of S and B are calculated by propagating the errors in the fitted parameters k_i and n_i and represent the 1σ standard error (s.e.) of the predicted values of S and B .

In Extended Data Fig. 6, the c_4 parameter along with its associated uncertainty for each source represent the median and 1σ dispersion of the posterior distribution. The values and uncertainties of the c_4 parameter for a subset of galaxies grouped by redshift, as well as the c_4 –redshift relation, are determined analogously to the B parameter in Fig. 3b.

We have compared the V-band attenuation, A_v , derived from SED fitting to values from the Balmer decrement, A_v^{BD} . We find that over 25% of the galaxies in the sample are characterized by negative A_v^{BD} (refs. 46, 94, 95) values. This non-physical result arises from observed line ratios that are lower or comparable to the intrinsic value of 2.86–2.87 (ref. 96).

The Balmer line ratio can be affected by various issues, including low spectral resolution, poor line fits, assumptions on empirical relations (for example, H α /N II line ratio) and physical conditions (for example, temperature and gas density)^{97, 98} at high- z that differ from

the standard ones⁹⁶. Therefore, for consistency and reliability, we have used A_V estimates obtained from SED fitting.

Comparison with the literature

In Fig. 3, we report the literature findings for the slope S and the bump B . The MW²³ and SMC²² are indicated by blue dotted lines. Other local individual sources—M31 (ref. 99), M33 (ref. 100), M51 (ref. 101) and M74 (ref. 102) are depicted as blue \times symbols. The median/mean values of samples of nearby ($z \approx 0$) and intermediate- z ($z \approx 1$ –4) galaxies from various studies^{21,42–46,48,103–107} are represented by green \times symbols. Slopes for subsamples of low- and intermediate- z galaxies are shown as magenta⁸⁹ and cyan⁴⁷ \times symbols, respectively. Finally, individual high- z ($z \approx 4$ –8) sources are indicated by violet¹⁴, olive¹⁶ and orange \times symbols¹⁵.

Literature results for all the local sources and most nearby^{21,103–106} and intermediate- z ^{42–46,50} galaxy samples are directly adopted from the work of ref. 2. Specific literature values of S and B are recalculated from their original parametrizations using the relations provided by ref. 2. For instance, certain studies⁸⁹ utilize the parametrization from ref. 54, $A_\lambda/A_V = (\lambda/0.55\text{ }\mu\text{m})^{-n}$, where the power law exponent n characterizes the UV-optical slope. In such cases, we make use of the relation $\log S = n/1.772$ to convert to the S parameter. In works that use the ref. 50 parametrization^{50,107} and the δ parameter to parametrize the slope, we use the relation $\log S = 0.4 - 0.55\delta$. Reference 47 uses the parametrization of ref. 104 and provides a relation to convert to the parametrization of ref. 108. Finally, the remaining literature results^{15,16,48,107} are directly provided by the authors.

To date, the detection of the characteristic 2,175 Å feature has been reported in two galaxies at $z \approx 7$ (refs. 15,16), both of which are also a part of the DAWN sample. Reference 16 reported a UV bump detection (with a 6.4σ) in the JADES-GS-z6-0 galaxy, achieved by fitting an excess attenuation centred at 2,236 Å with a Drude profile. However, applying our method (but setting the central wavelength of the bump to 2,236 Å to match the peak wavelength of the UV bump reported in their study) to the full spectrum of JADES-GS-z6-0 from JADES resulted in a marginal detection, with a UV bump strength of $B = 0.134 \pm 0.067$ or $c_4 = 0.020^{+0.012}_{-0.011}$ (-2σ). However, our model assumes a UV bump width that is approximately twice as large as the value used in ref. 16. Differences in the assumed bump width between the two studies could explain the variation in results.

Next, in our recent study¹⁵, we reported a hint of a UV bump detection in one out of three high- z sources, s00717, at $z \approx 6.9$, with a UV bump strength of $c_4 = 0.033^{+0.013}_{-0.012}$ (-2.7σ). Employing the identical SED fitting method with the same set of priors¹⁵ on the DAWN observations of the s00717 source yields $c_4 = 0.019^{+0.031}_{-0.017}$.

Inconsistencies in these results may arise from the use of various fitting procedures involving different models (for JADES-GS-z6-0) as well as different data reduction pipelines generating slightly different final one-dimensional spectra (for s00717). For s00717, the data reduction in our previous work was performed with the standard pipeline¹⁰⁹, whereas the data in this work are reduced with the MSAEXP custom code⁷⁵. The different pipeline versions have different sampling, resulting in slightly different flux densities, uncertainties and channel widths, which can create inconsistencies. When investigating the redshift evolution of galaxy properties, it is thus recommended to adopt samples of galaxies for which the data reduction analysis is performed with the same pipeline, as in the case of our study.

Observational and model uncertainties

Factors that could contribute to the discrepancy in slopes between our study and the ones from the literature at $z \approx 2$ can arise both from observational uncertainties and from model dependencies. Regarding the observational uncertainties, at the low redshift limit of our sample ($z \approx 2$ –2.8), NIRSpec prism observations ($\lambda \approx 0.6$ –5.3 μm) are restricted to the rest-frame $\lambda \geq 1,600$ –2,000 Å, which probe the UV bump peak and marginally extend into the far-UV rise of the attenuation curve. This

constraint in wavelength coverage may contribute to larger uncertainties in inferred slopes (Fig. 2). Moreover, for $z \approx 2$ –2.8 sources, NIRSpec data are probing the attenuation curve with a fraction of the spectra at shorter wavelengths, which suffer from larger uncertainties, due to the lower resolution ($R \approx \lambda/\Delta\lambda \approx 50$) of the NIRSpec prism disperser in the wavelength range of $\lambda_{\text{obs}} \approx 0.5$ –2 μm. Finally, the observed discrepancy may be attributed to the lower number of sources per bin at intermediate redshifts (13–21 sources) compared to the higher redshift bins (20–66 objects).

Regarding the model dependencies, different SED fitting codes with different sets of model prescriptions (SFHs^{15,110,111}, dust attenuation, Stellar Population Synthesis and initial mass function^{112,113}) and imposed priors on parameters^{43,47} can have an important impact on the output parameters, including the recovered attenuation curve. We conducted extensive testing of our customized SED fitting tool with seven different SFH models¹⁵. Our analysis revealed that although the choice of SFH model can influence properties closely linked to the SFH itself (for example, M^* , SFR and $\langle a \rangle^m$), the constrained dust attenuation properties remain largely unaffected by the assumed SFH. This finding underscores the robustness of our results concerning dust attenuation, irrespective of the specific SFH model employed.

Data availability

The data analysed in this study can be accessed at <https://dawn-cph.github.io/dja/index.html>. The data generated during this study, including basic galaxy properties and dust attenuation curve parameters, are provided with this manuscript (Supplementary Data 1 file). The complete source dataset of global galaxy properties derived from our SED fitting method is available upon request, as these will be the focus of a detailed analysis in an upcoming follow-up study.

Code availability

MSAEXP MSA spectra⁷⁵ and BAGPIPES⁴¹ Python scripts are publicly available at <https://github.com/gbammer/msaexp> and <https://github.com/ACCarnall/bagpipes>, respectively. The AstroPy¹¹⁴, MultiNest¹¹⁵ and PyMultiNest¹¹⁶ software packages are publicly available at <https://github.com/astropy/astropy>, <https://github.com/JohannesBuchner/MultiNest?tab=readme-ov-file> and <https://github.com/JohannesBuchner/PyMultiNest>, respectively.

References

- Calzetti, D. Star formation rate indicators. In *Secular Evolution of Galaxies* (eds Falcón-Barroso, J. & Knapen, J. H.) 419–458 (Cambridge University Press, 2013).
- Salim, S. & Narayanan, D. The dust attenuation law in galaxies. *Annu. Rev. Astron. Astrophys.* **58**, 529–575 (2020).
- Mathis, J. S., Rumpl, W. & Nordsieck, K. H. The size distribution of interstellar grains. *Astrophys. J.* **217**, 425–433 (1977).
- Draine, B. T. & Lee, H. M. Optical properties of interstellar graphite and silicate grains. *Astrophys. J.* **285**, 89–108 (1984).
- Weingartner, J. C. & Draine, B. T. Dust grain-size distributions and extinction in the Milky Way, Large Magellanic Cloud, and Small Magellanic Cloud. *Astrophys. J.* **548**, 296–309 (2001).
- Stecher, T. P. Interstellar extinction in the ultraviolet. *Astrophys. J.* **142**, 1683–1684 (1965).
- Desert, F. X., Boulanger, F. & Puget, J. L. Interstellar dust models for extinction and emission. *Astron. Astrophys.* **237**, 215–236 (1990).
- Siebenmorgen, R. & Kruegel, E. Dust model containing polycyclic aromatic hydrocarbons in various environments. *Astron. Astrophys.* **259**, 614–626 (1992).
- Chevallard, J., Charlot, S., Wandelt, B. & Wild, V. Insights into the content and spatial distribution of dust from the integrated spectral properties of galaxies. *Mon. Not. R. Astron. Soc.* **432**, 2061–2091 (2013).

10. Battisti, A. J., Cunha, E. D., Shvarei, I. & Calzetti, D. The strength of the 2175 Å feature in the attenuation curves of galaxies at $0.1 < z \lesssim 3$. *Astrophys. J.* **888**, 108–123 (2020).

11. Narayanan, D., Conroy, C., Davé, R., Johnson, B. D. & Popping, G. A theory for the variation of dust attenuation laws in galaxies. *Astrophys. J.* **869**, 70–91 (2018).

12. Trayford, J. W., Lagos, Cd. P., Robotham, A. S. G. & Obreschkow, D. Fade to grey: systematic variation of galaxy attenuation curves with galaxy properties in the EAGLE simulations. *Mon. Not. R. Astron. Soc.* **491**, 3937–3951 (2020).

13. Ferrara, A., Bianchi, S., Cimatti, A. & Giovanardi, C. An atlas of Monte Carlo models of dust extinction in galaxies for cosmological applications. *Astrophys. J. Suppl. Ser.* **123**, 437–445 (1999).

14. Boquien, M. et al. The ALPINE-ALMA [C II] survey. Dust attenuation curves at $z = 4.4\text{--}5.5$. *Astron. Astrophys.* **663**, A50–A68 (2022).

15. Markov, V. et al. Dust attenuation law in JWST galaxies at $z \sim 7\text{--}8$. *Astron. Astrophys.* **679**, A12–A33 (2023).

16. Witstok, J. et al. Carbonaceous dust grains seen in the first billion years of cosmic time. *Nature* **621**, 267–270 (2023).

17. Gallerani, S. et al. The extinction law at high redshift and its implications. *Astron. Astrophys.* **523**, A85–A107 (2010).

18. Di Mascia, F. et al. The dust attenuation law in $z \gtrsim 6$ quasars. *Mon. Not. R. Astron. Soc.* **506**, 3946–3961 (2021).

19. Stratta, G., Gallerani, S. & Maiolino, R. Is GRB 050904 at $z = 6.3$ absorbed by dust? *Astron. Astrophys.* **532**, A45–A53 (2011).

20. Bolmer, J. et al. Dust reddening and extinction curves toward gamma-ray bursts at $z > 4$. *Astron. Astrophys.* **609**, A62–A87 (2018).

21. Calzetti, D. et al. The dust content and opacity of actively star-forming galaxies. *Astrophys. J.* **533**, 682–695 (2000).

22. Gordon, K. D., Clayton, G. C., Misselt, K. A., Landolt, A. U. & Wolff, M. J. A quantitative comparison of the Small Magellanic Cloud, Large Magellanic Cloud, and Milky Way ultraviolet to near-infrared extinction curves. *Astrophys. J.* **594**, 279–293 (2003).

23. Cardelli, J. A., Clayton, G. C. & Mathis, J. S. The relationship between infrared, optical, and ultraviolet extinction. *Astrophys. J.* **345**, 245–256 (1989).

24. Boyer, M. L. et al. An infrared census of dust in nearby galaxies with Spitzer (DUSTINGS). IV. Discovery of high-redshift AGB analogs. *Astrophys. J.* **851**, 152–166 (2017).

25. Burgarella, D. et al. Observational and theoretical constraints on the formation and early evolution of the first dust grains in galaxies at $5 < z < 10$. *Astron. Astrophys.* **637**, A32–A48 (2020).

26. Spitzer, L. *Physical Processes in the Interstellar Medium* (Wiley, 1978).

27. Dwek, E. & Scalo, J. M. The evolution of refractory interstellar grains in the solar neighborhood. *Astrophys. J.* **239**, 193–211 (1980).

28. Ferrara, A. et al. A physical model for [C II] line emission from galaxies. *Mon. Not. R. Astron. Soc.* **489**, 1–12 (2019).

29. Pallottini, A. et al. Deep into the structure of the first galaxies: SERRA views. *Mon. Not. R. Astron. Soc.* **487**, 1689–1708 (2019).

30. Pallottini, A. et al. A survey of high- z galaxies: SERRA simulations. *Mon. Not. R. Astron. Soc.* **513**, 5621–5641 (2022).

31. Vallini, L., Ferrara, A., Pallottini, A., Carniani, S. & Gallerani, S. Star formation law in the epoch of reionization from [C II] and C III] lines. *Mon. Not. R. Astron. Soc.* **495**, L22–L26 (2020).

32. Markov, V. et al. The interstellar medium of high-redshift galaxies: gathering clues from C III] and [C II] lines. *Astron. Astrophys.* **663**, A172–A188 (2022).

33. Förster Schreiber, N. M. et al. The SINS survey: SINFONI integral field spectroscopy of $z \sim 2$ star-forming galaxies. *Astrophys. J.* **706**, 1364–1428 (2009).

34. Meštrić, U. et al. Exploring the physical properties of lensed star-forming clumps at $2 \lesssim z \lesssim 6$. *Mon. Not. R. Astron. Soc.* **516**, 3532–3555 (2022).

35. Ferrara, A., Pallottini, A. & Dayal, P. On the stunning abundance of super-early, luminous galaxies revealed by JWST. *Mon. Not. R. Astron. Soc.* **522**, 3986–3991 (2023).

36. Pallottini, A. & Ferrara, A. Stochastic star formation in early galaxies: implications for the James Webb Space Telescope. *Astron. Astrophys.* **677**, L4–L10 (2023).

37. Behrens, C., Pallottini, A., Ferrara, A., Gallerani, S. & Vallini, L. Dusty galaxies in the Epoch of Reionization: simulations. *Mon. Not. R. Astron. Soc.* **477**, 552–565 (2018).

38. Carniani, S. et al. Kiloparsec-scale gaseous clumps and star formation at $z = 5\text{--}7$. *Mon. Not. R. Astron. Soc.* **478**, 1170–1184 (2018).

39. Markov, V. et al. Massive molecular gas reservoir around the central AGN in the CARLA J103 + 3449 cluster at $z = 1.44$. *Astron. Astrophys.* **641**, A22–A39 (2020).

40. Sommovigo, L. et al. A new look at the infrared properties of $z \sim 5$ galaxies. *Mon. Not. R. Astron. Soc.* **517**, 5930–5941 (2022).

41. Carnall, A. C., McLure, R. J., Dunlop, J. S. & Davé, R. Inferring the star formation histories of massive quiescent galaxies with BAGPIPES: evidence for multiple quenching mechanisms. *Mon. Not. R. Astron. Soc.* **480**, 4379–4401 (2018).

42. Buat, V. et al. GOODS-Herschel: evidence of a UV extinction bump in galaxies at $z > 1$. *Astron. Astrophys.* **533**, A93–A109 (2011).

43. Buat, V. et al. GOODS-Herschel: dust attenuation properties of UV selected high redshift galaxies. *Astron. Astrophys.* **545**, A141–A156 (2012).

44. Kriek, M. & Conroy, C. The dust attenuation law in distant galaxies: evidence for variation with spectral type. *Astrophys. J. Lett.* **775**, L16–L22 (2013).

45. Scoville, N. et al. Dust attenuation in high redshift galaxies: ‘diamonds in the sky’. *Astrophys. J.* **800**, 108–114 (2015).

46. Reddy, N. A. et al. The MOSDEF survey: measurements of Balmer decrements and the dust attenuation curve at redshifts $z \sim 1.4\text{--}2.6$. *Astrophys. J.* **806**, 259–283 (2015).

47. Tress, M. et al. SHARDS: constraints on the dust attenuation law of star-forming galaxies at $z \sim 2$. *Mon. Not. R. Astron. Soc.* **475**, 2363–2374 (2018).

48. Shvarei, I. et al. The MOSDEF survey: the variation of the dust attenuation curve with metallicity. *Astrophys. J.* **899**, 117–136 (2020).

49. Li, A. et al. On dust extinction of gamma-ray burst host galaxies. *Astrophys. J.* **685**, 1046–1051 (2008).

50. Noll, S. et al. GMASS ultradeep spectroscopy of galaxies at $z \sim 2$. IV. The variety of dust populations. *Astron. Astrophys.* **499**, 69–85 (2009).

51. Conroy, C. Modeling the panchromatic spectral energy distributions of galaxies. *Annu. Rev. Astron. Astrophys.* **51**, 393–455 (2013).

52. Salmon, B. et al. Breaking the curve with CANDELS: a Bayesian approach to reveal the non-universality of the dust-attenuation law at high redshift. *Astrophys. J.* **827**, 20–39 (2016).

53. Hsu, Y.-M., Hirashita, H., Lin, Y.-H., Camps, P. & Baes, M. Effects of dust sources on dust attenuation properties in IllustrisTNG galaxies at $z \sim 7$. *Mon. Not. R. Astron. Soc.* **519**, 2475–2485 (2023).

54. Charlot, S. & Fall, S. M. A simple model for the absorption of starlight by dust in galaxies. *Astrophys. J.* **539**, 718–731 (2000).

55. Zanella, A. et al. A contribution of star-forming clumps and accreting satellites to the mass assembly of $z \sim 2$ galaxies. *Mon. Not. R. Astron. Soc.* **489**, 2792–2818 (2019).

56. Fujimoto, S. et al. Primordial rotating disk composed of ~ 15 dense star-forming clumps at cosmic dawn. Preprint at <https://arxiv.org/abs/2402.18543> (2024).

57. Adamo, A. et al. Bound star clusters observed in a lensed galaxy 460 Myr after the Big Bang. *Nature* **632**, 513–516 (2024).

58. McKinnon, R., Vogelsberger, M., Torrey, P., Marinacci, F. & Kannan, R. Simulating galactic dust grain evolution on a moving mesh. *Mon. Not. R. Astron. Soc.* **478**, 2851–2886 (2018).

59. Hirashita, H. & Murga, M. S. Self-consistent modelling of aromatic dust species and extinction curves in galaxy evolution. *Mon. Not. R. Astron. Soc.* **492**, 3779–3793 (2020).

60. Makiya, R. & Hirashita, H. Cosmic evolution of grain size distribution in galaxies using the v^2 GC semi-analytical model. *Mon. Not. R. Astron. Soc.* **517**, 2076–2087 (2022).

61. Todini, P. & Ferrara, A. Dust formation in primordial Type II supernovae. *Mon. Not. R. Astron. Soc.* **325**, 726–736 (2001).

62. Nozawa, T. et al. Evolution of dust in primordial supernova remnants: can dust grains formed in the ejecta survive and be injected into the early interstellar medium? *Astrophys. J.* **666**, 955–966 (2007).

63. Gall, C. et al. Rapid formation of large dust grains in the luminous supernova 2010jl. *Nature* **511**, 326–329 (2014).

64. Asano, R. S., Takeuchi, T. T., Hirashita, H. & Inoue, A. K. Dust formation history of galaxies: a critical role of metallicity for the dust mass growth by accreting materials in the interstellar medium. *Earth Planets Space* **65**, 213–222 (2013).

65. Asano, R. S., Takeuchi, T. T., Hirashita, H. & Nozawa, T. What determines the grain size distribution in galaxies? *Mon. Not. R. Astron. Soc.* **432**, 637–652 (2013).

66. Tazaki, R. & Ichikawa, K. Dust destruction by drift-induced sputtering in active galactic nuclei. *Astrophys. J.* **892**, 149–163 (2020).

67. Tazaki, R., Ichikawa, K. & Kokubo, M. Dust destruction by charging: a possible origin of gray extinction curves of active galactic nuclei. *Astrophys. J.* **892**, 84–90 (2020).

68. Gall, C. & Hjorth, J. Maximally dusty star-forming galaxies: supernova dust production and recycling in local group and high-redshift galaxies. *Astrophys. J.* **868**, 62–72 (2018).

69. Winters, J. M., Fleischer, A. J., Le Bertre, T. & Sedlmayr, E. Circumstellar dust shells around long-period variables. V. A consistent time-dependent model for the extreme carbon star AFGL 3068. *Astron. Astrophys.* **326**, 305–317 (1997).

70. Ferrarotti, A. S. & Gail, H. P. Composition and quantities of dust produced by AGB-stars and returned to the interstellar medium. *Astron. Astrophys.* **447**, 553–576 (2006).

71. Leśniewska, A. & Michałowski, M. J. Dust production scenarios in galaxies at $z \sim 6$ –8.3. *Astron. Astrophys.* **624**, L13–L18 (2019).

72. Dubois, Y. et al. Galaxies with grains: unraveling dust evolution and extinction curves with hydrodynamical simulations. *Astron. Astrophys.* **687**, A240–A270 (2024).

73. Maiolino, R. et al. A supernova origin for dust in a high-redshift quasar. *Nature* **431**, 533–535 (2004).

74. Brammer, G. Dawn JWST archive. DJA <https://dawn-cph.github.io/dja/index.html> (2023).

75. Brammer, G. MSAEXP: NIRSpec analysis tools. Zenodo <https://doi.org/10.5281/zenodo.7299500> (2022).

76. JWST user documentation. JWST <https://jwst-docs.stsci.edu/jwst-near-infrared-spectrograph/nirspec-operations/nirspec-mos-operations/nirspec-mos-operations-slit-losses> (2017).

77. Beck, T. L. et al. Planning JWST NIRSpec MSA spectroscopy using NIRCam pre-images. In *Proc. SPIE 9910, Observatory Operations: Strategies, Processes, and Systems VI* (eds Peck, A. B. et al.) 99101O (SPIE, 2016); <https://doi.org/10.1117/12.2232804>

78. Franco, M. et al. GOODS-ALMA: 1.1 mm galaxy survey. I. Source catalog and optically dark galaxies. *Astron. Astrophys.* **620**, A152–A178 (2018).

79. Dunlop, J. S. et al. A deep ALMA image of the Hubble Ultra Deep Field. *Mon. Not. R. Astron. Soc.* **466**, 861–883 (2017).

80. Hatsukade, B. et al. ALMA twenty-six arcmin² survey of GOODS-S at one millimeter (ASAGAO): source catalog and number counts. *Publ. Astron. Soc. Jpn* **70**, 105–124 (2018).

81. Gómez-Guijarro, C. et al. GOODS-ALMA 2.0: source catalog, number counts, and prevailing compact sizes in 1.1 mm galaxies. *Astron. Astrophys.* **658**, A43–A72 (2022).

82. Fujimoto, S. et al. DUALZ: Deep UNCOVER-ALMA Legacy High-Z Survey. Preprint at <https://arxiv.org/abs/2309.07834> (2023).

83. Sun, F. et al. ALMA lensing cluster survey: ALMA-Herschel joint study of lensed dusty star-forming galaxies across $z = 0.5$ –6. *Astrophys. J.* **932**, 77–113 (2022).

84. Chevallard, J. & Charlot, S. Modelling and interpreting spectral energy distributions of galaxies with beagle. *Mon. Not. R. Astron. Soc.* **462**, 1415–1443 (2016).

85. Ferland, G. J. et al. The 2017 release cloudy. *Rev. Mexicana Astron. Astrofis.* **53**, 385–438 (2017).

86. Inoue, A. K., Shimizu, I., Iwata, I. & Tanaka, M. An updated analytic model for attenuation by the intergalactic medium. *Mon. Not. R. Astron. Soc.* **442**, 1805–1820 (2014).

87. Leja, J., Carnall, A. C., Johnson, B. D., Conroy, C. & Speagle, J. S. How to measure galaxy star formation histories. II. Nonparametric models. *Astrophys. J.* **876**, 3–27 (2019).

88. Topping, M. W. et al. The ALMA REBELS survey: specific star formation rates in the reionization era. *Mon. Not. R. Astron. Soc.* **516**, 975–991 (2022).

89. Salim, S., Boquien, M. & Lee, J. C. Dust attenuation curves in the local universe: demographics and new laws for star-forming galaxies and high-redshift analogs. *Astrophys. J.* **859**, 11–28 (2018).

90. Draine, B. On the interpretation of the $\lambda 2175$ Å feature. In *Interstellar dust Vol. 135* (eds Allamandola, L. J. & Tielens, A. G. G. M.) 313–327 (International Astronomical Union, 1989).

91. Shavvai, I. et al. The UV 2175Å attenuation bump and its correlation with PAH emission at $z \sim 2$. *Mon. Not. R. Astron. Soc.* **514**, 1886–1894 (2022).

92. Feroz, F., Hobson, M. P., Cameron, E. & Pettitt, A. N. Importance nested sampling and the multinest algorithm. *Open J. Astrophys.* **2**, 10–38 (2019).

93. Lucy, L. B. Frequentist tests for Bayesian models. *Astron. Astrophys.* **588**, A19–A27 (2016).

94. Matharu, J. et al. A first look at spatially resolved Balmer decrements at $1.0 < z < 2.4$ from JWST NIRISS slitless spectroscopy. *Astrophys. J. Lett.* **949**, L11–L18 (2023).

95. Sandles, L. et al. JADES: Balmer decrement measurements at redshifts $4 < z < 7$. Preprint at <https://arxiv.org/abs/2306.03931> (2023).

96. Osterbrock, D. E. & Ferland, G. J. *Astrophysics of Gaseous Nebulae and Active Galactic Nuclei* (University Science Books, 2006).

97. Curti, M. et al. The chemical enrichment in the early Universe as probed by JWST via direct metallicity measurements at $z \sim 8$. *Mon. Not. R. Astron. Soc.* **518**, 425–438 (2023).

98. Reddy, N. A., Topping, M. W., Sanders, R. L., Shapley, A. E. & Brammer, G. A JWST/NIRSpec exploration of the connection between ionization parameter, electron density, and star-formation-rate surface density in $z = 2.7$ –6.3 galaxies. *Astrophys. J.* **952**, 167–182 (2023).

99. Viaene, S. et al. The Herschel Exploitation of Local Galaxy Andromeda (HELGA). VII. A SKIRT radiative transfer model and insights on dust heating. *Astron. Astrophys.* **599**, A64–A86 (2017).

100. Williams, T. G. et al. High-resolution radiative transfer modelling of M33. *Mon. Not. R. Astron. Soc.* **487**, 2753–2770 (2019).

101. De Looze, I. et al. High-resolution, 3D radiative transfer modeling. I. The grand-design spiral galaxy M 51. *Astron. Astrophys.* **571**, A69–A92 (2014).

102. Decleir, M. et al. Revealing the dust attenuation properties on resolved scales in NGC 628 with SWIFT UVOT data. *Mon. Not. R. Astron. Soc.* **486**, 743–767 (2019).

103. Burgarella, D., Buat, V. & Iglesias-Páramo, J. Star formation and dust attenuation properties in galaxies from a statistical ultraviolet-to-far-infrared analysis. *Mon. Not. R. Astron. Soc.* **360**, 1413–1425 (2005).

104. Conroy, C., Schiminovich, D. & Blanton, M. R. Dust attenuation in disk-dominated galaxies: evidence for the 2175 Å dust feature. *Astrophys. J.* **718**, 184–198 (2010).

105. Wild, V. et al. Empirical determination of the shape of dust attenuation curves in star-forming galaxies. *Mon. Not. R. Astron. Soc.* **417**, 1760–1786 (2011).

106. Battisti, A. J., Calzetti, D. & Chary, R. R. Characterizing dust attenuation in local star-forming galaxies: UV and optical reddening. *Astrophys. J.* **818**, 13–37 (2016).

107. Decleir, M. *DustKING – Revealing the Dust Attenuation in Nearby Galaxies*. PhD thesis, Ghent University, Belgium (2019).

108. Noll, S. et al. Analysis of galaxy spectral energy distributions from far-UV to far-IR with CIGALE: studying a SINGS test sample. *Astron. Astrophys.* **507**, 1793–1813 (2009).

109. Jakobsen, P. et al. The Near-Infrared Spectrograph (NIRSpec) on the James Webb Space Telescope. I. Overview of the instrument and its capabilities. *Astron. Astrophys.* **661**, A80–A102 (2022).

110. Whitler, L. et al. Star formation histories of UV-luminous galaxies at $z = 6.8$: implications for stellar mass assembly at early cosmic times. *Mon. Not. R. Astron. Soc.* **519**, 5859–5881 (2023).

111. Tacchella, S. et al. JWST NIRCam + NIRSpec: interstellar medium and stellar populations of young galaxies with rising star formation and evolving gas reservoirs. *Mon. Not. R. Astron. Soc.* **522**, 6236–6249 (2023).

112. Katz, H. et al. The nature of high $[O\,III]_{88\mu m}/[C\,II]_{158\mu m}$ galaxies in the epoch of reionization: low carbon abundance and a top-heavy IMF? *Mon. Not. R. Astron. Soc.* **510**, 5603–5622 (2022).

113. Wang, B. et al. Quantifying the effects of known unknowns on inferred high-redshift galaxy properties: burstiness, IMF, and nebular physics. *Astrophys. J.* **963**, 74–89 (2024).

114. Astropy Collaboration. The Astropy project: sustaining and growing a community-oriented open-source project and the latest major release (v5.0) of the core package. *Astrophys. J.* **935**, 167–187 (2022).

115. Feroz, F., Hobson, M. P. & Bridges, M. MULTINEST: an efficient and robust Bayesian inference tool for cosmology and particle physics. *Mon. Not. R. Astron. Soc.* **398**, 1601–1614 (2009).

116. Buchner, J. et al. X-ray spectral modelling of the AGN obscuring region in the CDFS: Bayesian model selection and catalogue. *Astron. Astrophys.* **564**, A125–A150 (2014).

Acknowledgements

We would like to express our gratitude to H. Hirashita and I. Shvaei for engaging in productive discussions with us and providing valuable insights and comments. Additionally, we thank M. Decleir, I. Shvaei and J. Witstok for sharing their findings on the properties of the attenuation curve. V.M., A.F., A.P. and M.K. acknowledge support from the European Research Council (ERC) Advanced Grant INTERSTELLAR, grant no. H2020/740120. V.M. acknowledges support from the ERC

Grant FIRSTLIGHT and from the Slovenian National Research agency ARIS through grant nos. N1-0238 and P1-0188. Partial support (A.F.) from the Carl Friedrich von Siemens-Forschungspreis der Alexander von Humboldt-Stiftung Research Award is kindly acknowledged. Any dissemination of results must indicate that it reflects only the author's view and that the Commission is not responsible for any use that may be made of the information it contains. The data products presented herein were retrieved from the DJA. DJA is an initiative of the Cosmic Dawn Center, which is funded by the Danish National Research Foundation under grant no. 140. We gratefully acknowledge the computational resources of the Center for High Performance Computing (CHPC) at SNS.

Author contributions

V.M., S.G. and A.F. led the writing of this paper. E.P., V.M., M.K. and S.G. contributed to the target selection. V.M., E.P. and S.G. contributed to the visual inspection and additional data reduction. S.G., V.M. and A.P. contributed to the sample cleaning. V.M. led the SED fitting of the selected targets. S.G., V.M., A.F., A.P., L.S. and F.D.M. contributed to the development of the customized SED fitting tool. V.M., S.G., L.S., A.P., A.F. and M.K. contributed to the visualization of the results. V.M., S.G., A.P., M.K., A.F., E.P. and F.D.M. contributed to the analysis of the results. V.M., A.F., S.G. and A.P. contributed to the discussion on the physical interpretation of the results. All authors reviewed the manuscript.

Competing interests

The authors declare no competing interests.

Additional information

Extended data is available for this paper at <https://doi.org/10.1038/s41550-024-02426-1>.

Supplementary information The online version contains supplementary material available at <https://doi.org/10.1038/s41550-024-02426-1>.

Correspondence and requests for materials should be addressed to Vladan Markov, Simona Gallerani or Andrea Ferrara.

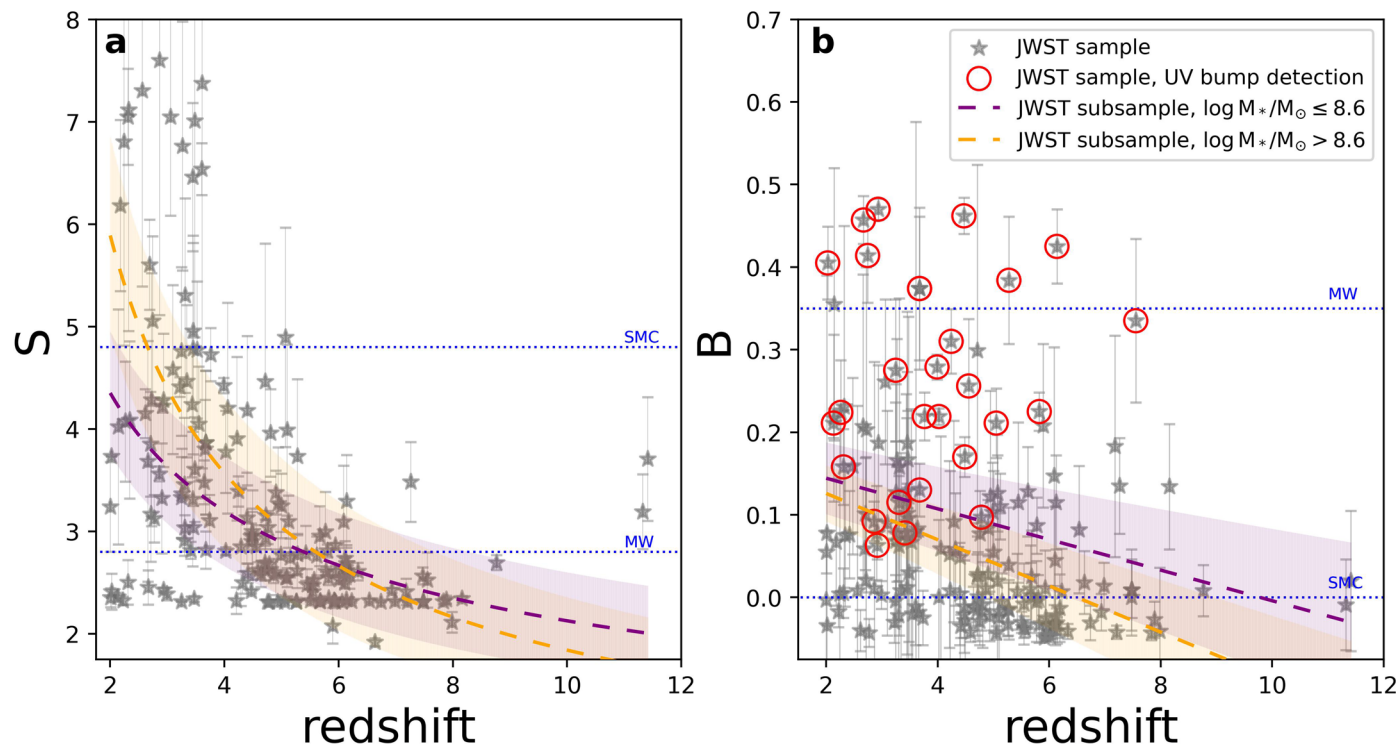
Peer review information *Nature Astronomy* thanks the anonymous reviewers for their contribution to the peer review of this work.

Reprints and permissions information is available at www.nature.com/reprints.

Publisher's note Springer Nature remains neutral with regard to jurisdictional claims in published maps and institutional affiliations.

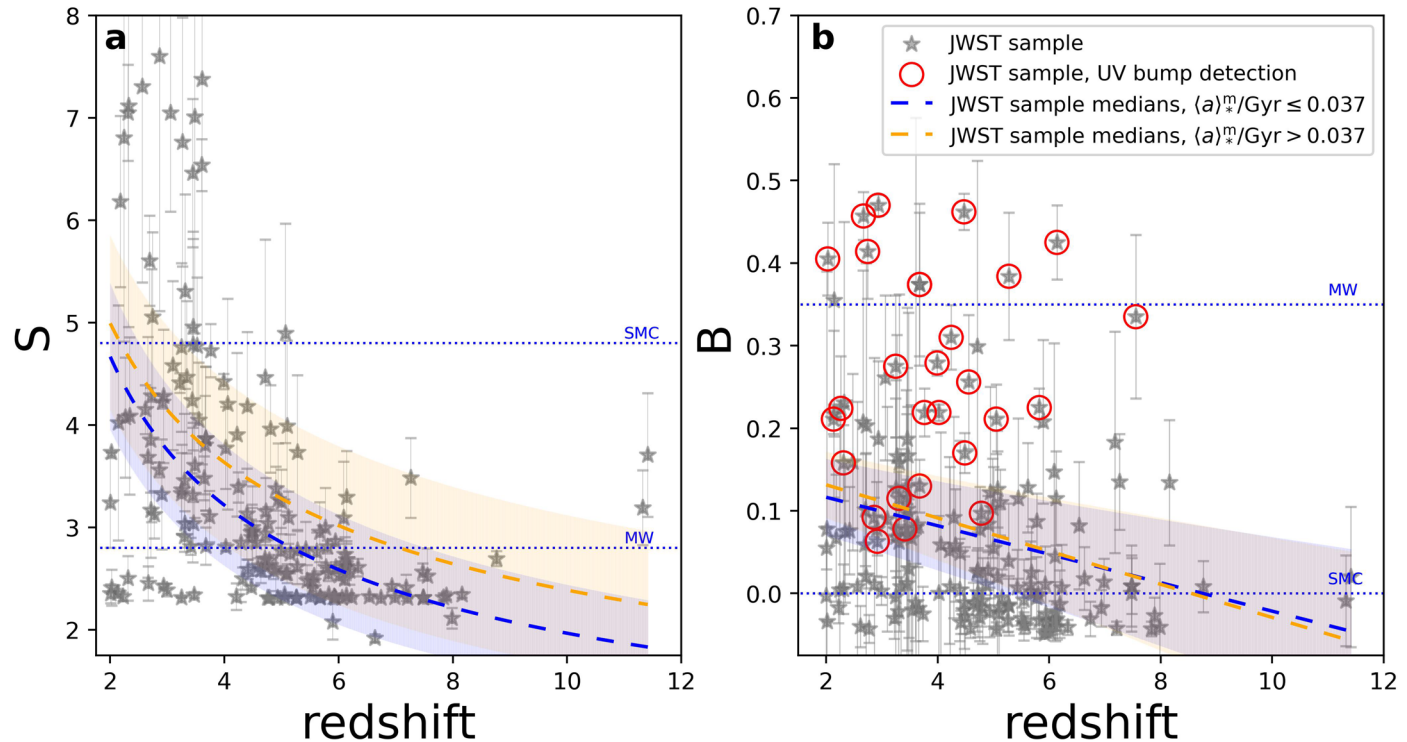
Springer Nature or its licensor (e.g. a society or other partner) holds exclusive rights to this article under a publishing agreement with the author(s) or other rightsholder(s); author self-archiving of the accepted manuscript version of this article is solely governed by the terms of such publishing agreement and applicable law.

© The Author(s), under exclusive licence to Springer Nature Limited 2025



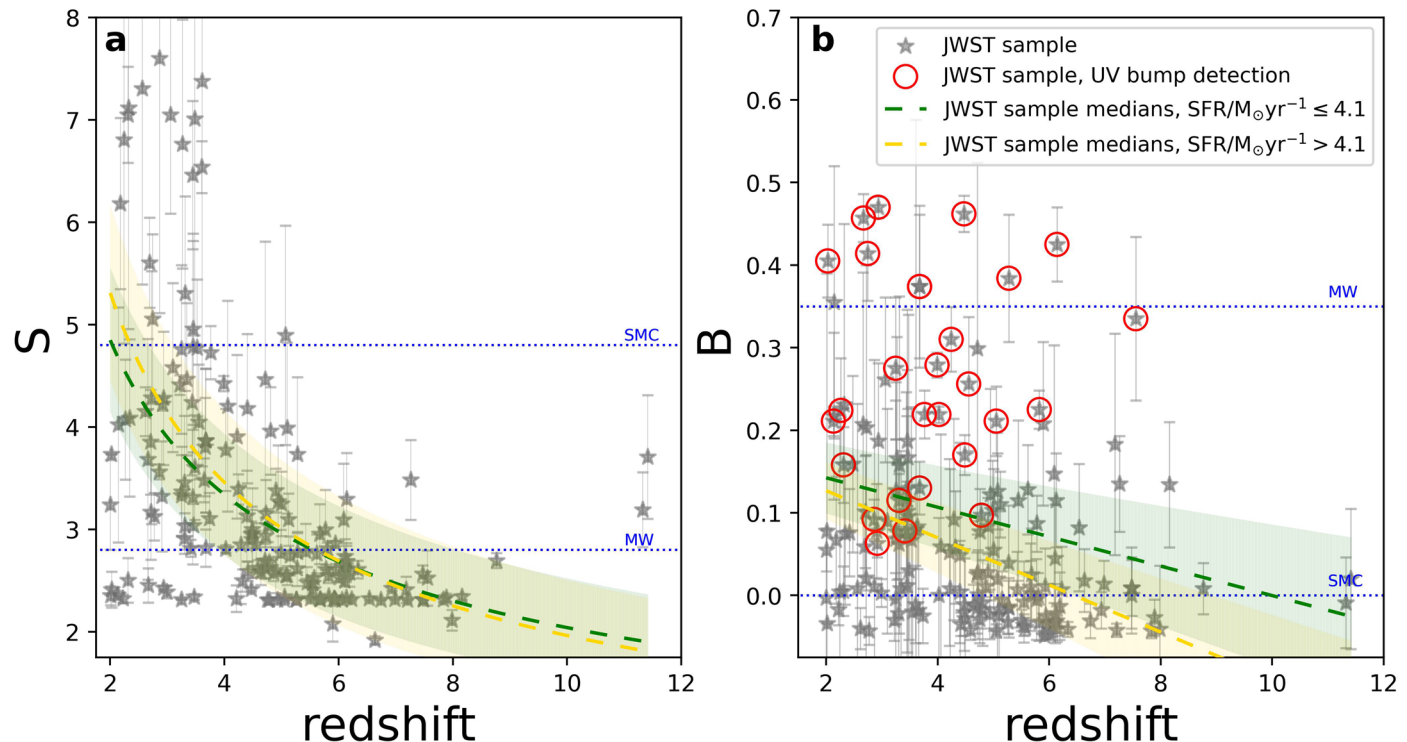
Extended Data Fig. 1 | Dust attenuation parameters as a function of redshift, binned by their stellar mass. **a**, UV-optical slope (S) versus redshift. **b**, UV bump strength (B) versus redshift. The S and B medians and their 1σ dispersions for individual sources are shown as grey stars and error bars. These medians and 1σ dispersions are obtained using a bootstrapping approach which involves generating attenuation curves from a random sampling of c1–c4 from the

posterior distribution (See Attenuation curve parametrization section). The purple and orange dashed lines and corresponding shaded regions depict the best fit and 1σ standard error (SE) for subsets of sources with $\log M_*/M_\odot \leq 8.6$ (87 sources) and $\log M_*/M_\odot > 8.6$ (86 sources), respectively, derived using the numpy polyfit function (See Attenuation curve parametrization section).



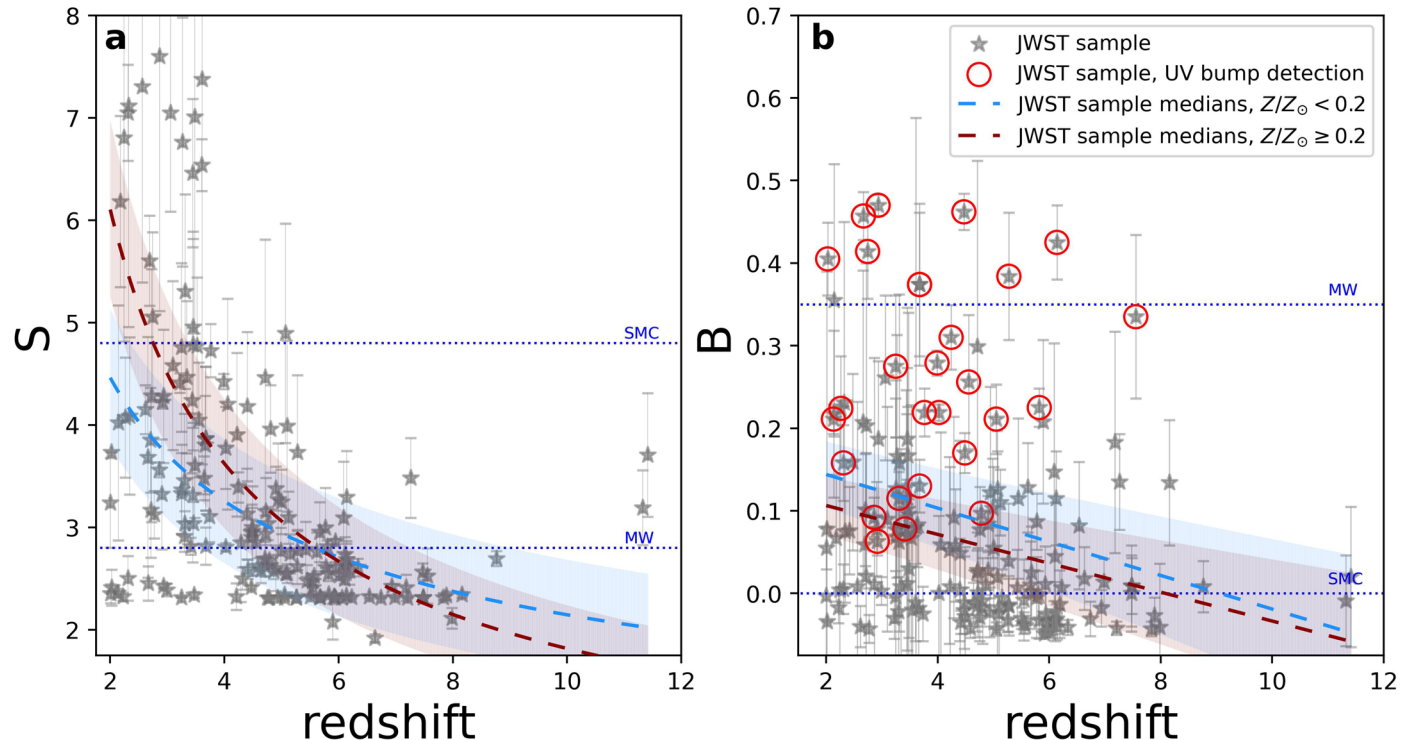
Extended Data Fig. 2 | Dust attenuation parameters as a function of redshift, binned by their mass-weighted stellar age. **a**, UV-optical slope (S) versus redshift. **b**, UV bump strength (B) versus redshift. The S and B medians and their 1σ dispersions for individual sources are shown as grey stars and error bars. These medians and 1σ dispersions are obtained using a bootstrapping approach which involves generating attenuation curves from a random sampling of c1 - c4 from

the posterior distribution (See Attenuation curve parametrization section). The blue and orange dashed lines and corresponding shaded regions depict the best fit and 1σ SE for subsets of sources with $\langle a \rangle_m^m / \text{Gyr} \leq 0.037$ (87 sources) and $\langle a \rangle_m^m / \text{Gyr} > 0.037$ (86 sources), respectively, derived using the numpy polyfit function (See Attenuation curve parametrization section).



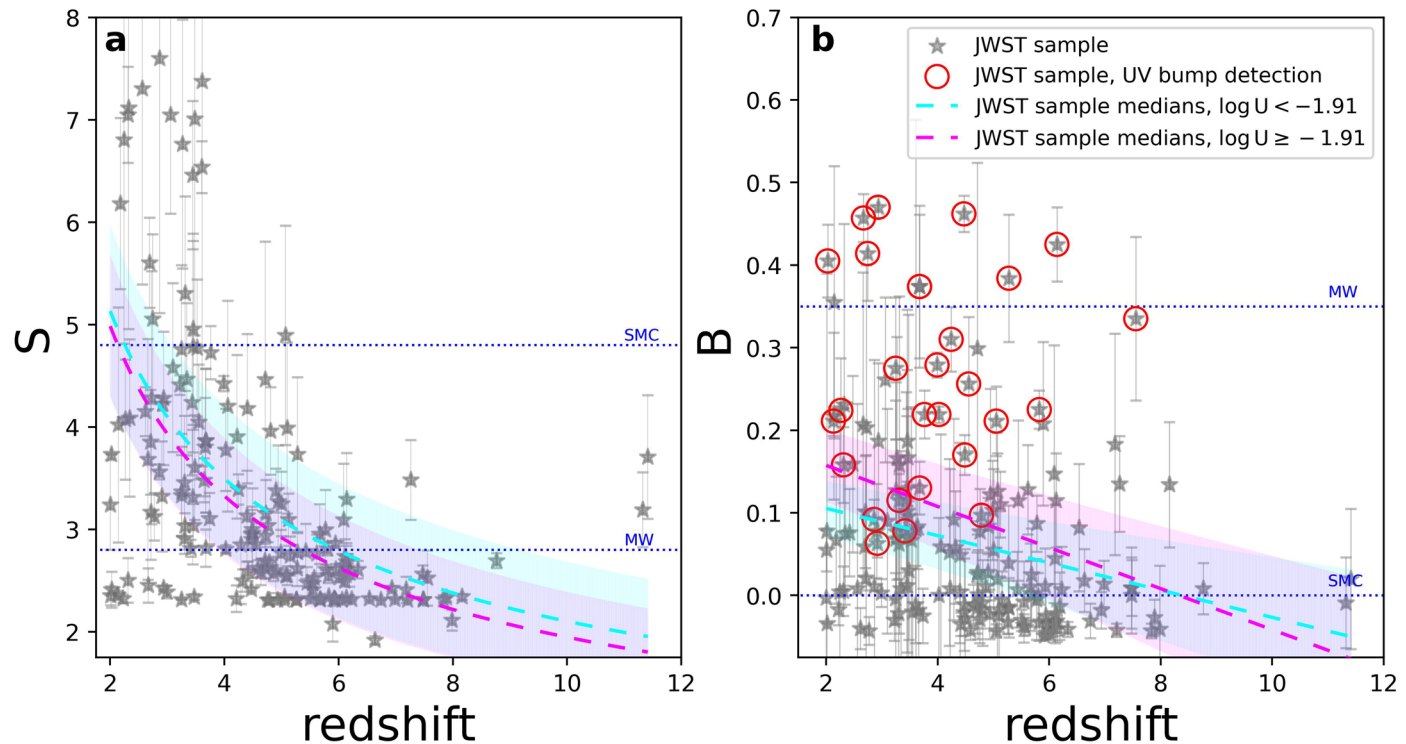
Extended Data Fig. 3 | Dust attenuation parameters as a function of redshift, binned by their SFR. **a**, UV-optical slope (S) versus redshift. **b**, UV bump strength (B) versus redshift. The S and B medians and their 1σ dispersions for individual sources are shown as grey stars and error bars. These medians and 1σ dispersions are obtained using a bootstrapping approach which involves generating attenuation curves from a random sampling of $c1 \cdot c4$ from the

posterior distribution (See Attenuation curve parametrization section). The green and gold dashed lines and corresponding shaded regions depict the best fit and 1σ SE for subsets of sources with $SFR/M_{\odot} \text{yr}^{-1} \leq 4.1$ (87 sources) and $SFR/M_{\odot} \text{yr}^{-1} > 4.1$ (86 sources), respectively, derived using the numpy polyfit function (See Attenuation curve parametrization section).



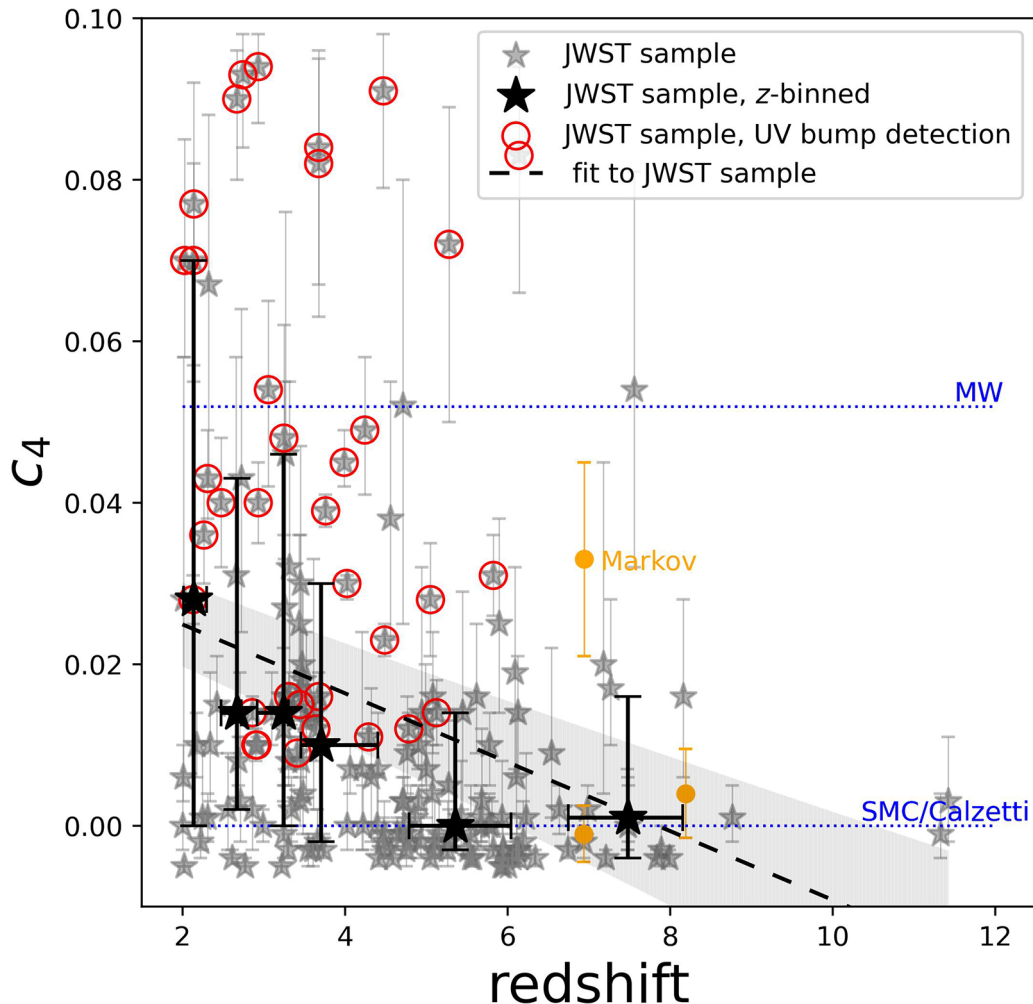
Extended Data Fig. 4 | Dust attenuation parameters as a function of redshift, binned by their metallicity. **a**, UV-optical slope (S) versus redshift. **b**, UV bump strength (B) versus redshift. The S and B medians and their 1σ dispersions for individual sources are shown as grey stars and error bars. These medians and 1σ dispersions are obtained using a bootstrapping approach which involves generating attenuation curves from a random sampling of $c1 - c4$ from the

posterior distribution (See Attenuation curve parametrization section). The light blue and dark red dashed lines and corresponding shaded regions depict the best fit and 1σ SE for subsets of sources with metallicities of $Z/Z_{\odot} < 0.199$ (85 sources) and $Z/Z_{\odot} \geq 0.199$ (88 sources), respectively, derived using the numpy polyfit function (See Attenuation curve parametrization section).



Extended Data Fig. 5 | Dust attenuation parameters as a function of redshift, binned by their ionization parameter. **a**, UV-optical slope (S) versus redshift. **b**, UV bump strength (B) versus redshift. The S and B medians and their 1σ dispersions for individual sources are shown as grey stars and error bars. These medians and 1σ dispersions are obtained using a bootstrapping approach which involves generating attenuation curves from a random sampling of c1-c4 from

the posterior distribution (See Attenuation curve parametrization section). The cyan and magenta dashed lines and corresponding shaded regions depict the best fit and 1σ SE for subsets of sources with $\log U < -1.91$ (87 sources) and $\log U \geq -1.91$ (86 sources), respectively, derived using the numpy polyfit function (See Attenuation curve parametrization section).



Extended Data Fig. 6 | UV bump strength, parametrized by the c_4 parameter, as a function of redshift. Our entire galaxy sample is represented by grey stars. The c_4 medians and their associated 1σ dispersions for individual sources are derived from the posterior distribution (See Attenuation curve parametrization section). Sources with UV bump detection are highlighted by red circles. The UV bump medians and corresponding 1σ dispersions for galaxies binned by redshift (corresponding to the redshift bins of Main Article Fig. 2) are indicated by

black stars with error bars. The median values and 1σ dispersions are estimated directly from the distribution of these parameters within each subset. The black dashed line and corresponding shaded region depict the best fit and 1σ SE for the entire sample, derived using the numpy polyfit function (See Attenuation curve parametrization section). Literature results are depicted as orange \times symbols with error bars representing their 1σ uncertainties (see the Comparison with the literature section).